
This manuscript is a preprint and has been submitted for publication in **Basin Research**. If accepted, the final version of this manuscript will be available via the '*Peer-reviewed Publication DOI*' link on the right-hand side of this webpage. Please feel free to contact any of the authors directly or to comment on the manuscript using **hypothes.is** (<https://web.hypothes.is/>). We welcome feedback!

1 Mass-transport complexes (MTCs) document subsidence patterns in 2 a northern Gulf of Mexico salt minibasin

3 Nan Wu¹, Christopher A-L. Jackson¹, Howard D. Johnson¹, David M. Hodgson², Harya D. Nugraha¹

4 ¹Basins Research Group (BRG), Department of Earth Science & Engineering, Imperial College, Prince
5 Consort Road, London, SW7 2BP, UK

6 ²School of Earth and Environment, University of Leeds, Leeds, LS2 9JT, UK

7 *Email: n.wu16@imperial.ac.uk

8 Abstract

9 Mass-transport complexes (MTCs) dominate the stratigraphic record of many salt-influenced
10 sedimentary basins. Commonly in such settings, halokinesis is invoked as a primary trigger for
11 MTC emplacement, although the link between specific phases of salt movement, and related
12 minibasin dynamics, remains unclear. Here, we use high-quality 3D seismic reflection and well
13 data to constrain the composition, geometry, and distribution (in time and space) of six MTCs
14 preserved in a salt-confined, supra-canopy minibasin in the northern Gulf of Mexico, and to
15 assess how their emplacement relate to regional and local controls. We define three main
16 tectono-sedimentary phases in the development of the minibasin: (1) initial minibasin
17 subsidence and passive diapirism, during which time deposition was dominated by relatively
18 large-volume MTCs (c. 25 km³) derived from the shelf-edge or upper slope; (2) minibasin
19 margin uplift and steepening, during which time small-volume MTCs (c. 20 km³) derived from
20 the shelf-edge or upper slope were emplaced; and (3) active diapirism, during which time very
21 small volume MTCs (c. 1 km³) were emplaced, locally derived from the diapir flanks or roofs.
22 We present a generic model that emphasises the dynamic nature of minibasin evolution, and
23 how MTC emplacement relates to halokinetic sequence development. Although based on a
24 single data-rich case study, our model may be applicable to other MTC-rich, salt-influenced
25 sedimentary basins.

26 Keywords: MTCs, salt mini-basins evolution, Gulf of Mexico.

27 Introduction

28 Mass-transport complexes (MTCs) are deposits of subaqueous mass flows, and comprise
29 slides, slumps, and debris-flows (Dott Jr, 1963; Nardin et al., 1979; Posamentier and Kolla,
30 2003). MTCs are found along all continental margins, and can play a major role in sediment

31 transfer from the continents to the deep ocean (e.g. Masson et al., 2006; Hjelstuen et al.,
32 2007; Talling et al., 2007; Li et al., 2015; Kioka et al., 2019). Seismic surveys image extremely
33 large (c. 20-1100 km³), now-buried MTCs (e.g. Gee et al., 1999; Frey Martinez et al., 2005;
34 Moscardelli et al., 2006; Sawyer et al., 2007; Moscardelli and Wood, 2008; Sawyer et al., 2009;
35 Ortiz - Karpf et al., 2016; Wu et al., 2019), showing they can constitute >50% of any given
36 deep-water stratigraphic succession (Posamentier and Walker, 2006). The failure process
37 leading to MTC emplacement can be externally preconditioned and triggered by earthquakes
38 and oversteepening of the slope (i.e. geometric preconditioning effects) (Nisbet and Piper,
39 1998; O'loughlin and Lander, 2003; Masson et al., 2010; Talling et al., 2014; Clare et al., 2016).
40 In addition to being stratigraphically important, the passage and emplacement of MTCs can
41 damage seabed infrastructure and can trigger tsunamis (Shipp, 2004; Harbitz et al., 2014). In
42 the petroleum industry, MTCs can serve as hydrocarbon seals and/or reservoirs (e.g.
43 Hampton et al., 1996; Locat and Lee, 2002; Weimer and Shipp, 2004; Wu et al., 2019).
44 Therefore, understanding the origin and morphological characteristics of MTCs is important
45 for societal and industrial reasons.

46 In salt-influenced sedimentary basins, uplift and subsidence associated with the flow of salt
47 is widely considered to be the primary control on slope failure and MTC emplacement (e.g.
48 Cashman and Popenoe, 1985; Moscardelli and Wood, 2008; Madof et al., 2009; Twichell et
49 al., 2009; Omosanya and Alves, 2013; Yeakley et al., 2019). However, there are additional
50 mechanisms to consider, including (i) formation of overpressure formation can be driven by
51 fluctuations in sedimentation rate, which are influenced by the location of the minibasin
52 relative to shelf-edge deltas and upper slope canyons; (ii) accommodation available at the
53 time of slope failure will dictate the volume of MTC-related material that is trapped and
54 preserved within any one minibasin, and the potential for sediment to be bypassed to more
55 distal depocentres; (iii) erosion, and ultimately undermining and failure of the depocentre
56 margins in response to the passage of near-bed currents (i.e. contour currents); (iv) failure of
57 contourite bodies; (iv) fluid migration and the generation of elevated pore pressures in
58 discrete sub-surface layers; this can reduce the vertical effective stress, thereby affecting
59 slope stability and potentially triggering slope failure; and (v) gas hydrate dissociation, which,
60 like pore pressure changes, can reduce sediment strength and trigger slope failure (Canals et

61 al., 2004; Kvalstad et al., 2005; Strout and Tjelta, 2005; Masson et al., 2010; Talling et al.,
62 2014).

63 Despite being volumetrically important, and although they can represent stratigraphic
64 markers for a range of basin-related processes, MTCs are not explicitly accounted for in
65 stratigraphic models for the salt-influenced slopes. Instead, turbidity current-fed systems
66 dominate in these models, presumably due to their association with reservoir-prone channels
67 and lobes, with the stratigraphic architecture and evolution of minibasins being primarily
68 described by the fill-and-spill model (Prather et al., 1998; Winker and Booth, 2000; Booth et
69 al., 2003; Mallarino et al., 2006; Madof et al., 2009; Prather et al., 2012). According to this
70 model, underfilled minibasins initially trap or 'pond' sediments before being overfilled; at this
71 point, when no more accommodation is available, sediment is bypassed to more distal
72 depocentres (Beaubouef and Friedmann, 2000; Booth et al., 2000; Booth et al., 2003).
73 Underlying this model are two major assumptions: (1) accommodation in the minibasin is
74 controlled by a steady-state, longitudinal bathymetric profile, and (2) the minibasin gradient
75 does not vary spatially and temporally during its evolution (Prather et al., 1998; Winker and
76 Booth, 2000; Mallarino et al., 2006). However, Madof et al. (2009) and Madof et al. (2017)
77 argue that these assumptions are unrealistic, given that minibasins can be extremely dynamic,
78 with their geometry, subsidence rate, and accommodation changing in response to variations
79 in sediment accumulation rate and input direction, and the rate and location of salt expulsion
80 from beneath their subsiding depocentres.

81 Motivated by the above discussion, we here use 3D seismic reflection and well data from the
82 northern Gulf of Mexico to: (i) define the geometry and emplacement mechanics of
83 minibasin-confined MTCs; and (ii) link MTC emplacement to the development of halokinetic
84 sequences (see below) that characterise specific stages in the relationship between minibasin
85 subsidence and sedimentation, and diapir uplift. By doing this, we can: (i) explicitly account
86 for MTCs in fill-and-spill models; (ii) characterise the longer-term, more dynamic interactions
87 occurring between deep-water sedimentary systems and salt-related slope topography; and
88 (iii) use MTCs as markers of salt-related structural deformation in deep-water. We focus on a
89 single upper slope minibasin in the northern Gulf of Mexico (Figure 1). However, the high-
90 quality dataset, and the fact that salt-sediment interactions have been documented in many

91 other sedimentary basins (e.g. Gulf of Mexico, offshore Brazil, offshore West Africa and East
92 Mediterranean), mean our findings are likely to be more broadly applicable.

93 Geological setting

94 Tectonics

95 The Gulf of Mexico passive continental margin formed in response to Triassic-Early
96 Cretaceous rifting (Pindell and Dewey, 1982; Salvador, 1987; Kneller and Johnson, 2011).
97 Rifting initiated during the Late Triassic, followed by repeated episodes of marine flooding of
98 a confined embayment during the Middle Jurassic. This led to the accumulation of the several
99 kilometre-thick Louann Salt (Diegel et al., 1995; Salazar et al., 2014). During the Mesozoic and
100 Cenozoic, large volumes of sediments were shed from the North American continent. This, in
101 concert with regional shortening, expelled the autochthonous salt into diapirs that fed a large,
102 allochthonous salt-canopy (Galloway et al., 2000). Numerous intraslope minibasins then
103 subsided into the canopy, in response to the differential loading by continent-derived
104 sediment, and kinematically linked extension and shortening of the supra-salt cover (Prather,
105 2000). Salt tectonics has thus been a major control on the stratigraphic evolution of the
106 northern Gulf of Mexico from the Miocene to Present (e.g. Madof et al., 2009).

107 Location of study area

108 The study area is located on the present northern Mississippi Slope, c. 60 km south-east of
109 the modern shelf-edge (Figure 1). This covers the upper slope, in a diapir- and minibasin-rich
110 region forming part of the larger, Plio-Pleistocene Mississippi Canyon/Fan System (Galloway
111 et al., 2000). Present water depths range from 1150 m in the SE to 650 m in the NW. Five
112 upper Pliocene to Holocene minibasins are imaged in our study area; we focus on the
113 Pleistocene fill of Minibasin 5, a c. 21 km long (N-S) by c. 8 km wide (E-W) depocentre, whose
114 base is c. 3600 m below the present seabed (Figure 2). Four salt diapirs bound the lateral
115 margins of Minibasin 5 (A-D; Figure 2), whereas a fifth diapir underlies it (E; Figure 3).

116 Dataset and methods

117 *Seismic reflection data*

118 The seismic reflection dataset used in this study covers an area of c. 550 km². The dataset was
119 acquired during 1995-1998 and reprocessed as a single survey in 2008. It contains a 3D zero-

120 phase, Kirchhoff pre-stack depth-migrated seismic reflection volume, with a vertical sample
121 rate of 10 m, record length of 15 km, and a final bin size of 25 m x 25 m. The vertical seismic
122 resolution is estimated to be c. 17-27 m (Wu et al., 2019).

123 We mapped nine key seismic horizons in a succession characterised by alternating packages
124 of high-amplitude, continuous reflections, and low-amplitude, more chaotic reflections
125 (Figure 3, 4). The mapped seismic horizons were selected based on their high-amplitude
126 response and good lateral continuity, and the fact that they bound seismic-stratigraphically
127 important packages that define specific tectono-sedimentary phases of minibasin
128 development (see below). We mapped eight additional horizons, each of which represented
129 the base or top surface of an MTC (e.g., H2.1, H5.1 in figure 3; see also Figures 4 and 5). We
130 used seismic attributes (i.e. variance and chaos), generated along or between these horizons,
131 to identify deep-water depositional elements. Variance and chaos attributes image spatial
132 discontinuities in seismic reflection events, which could relate to important structural (e.g.
133 intra-MTC faults) and/or stratigraphic discontinuities (e.g. the abrupt seismic facies change
134 from seismically chaotic MTCs to more continuous slope strata) (Chopra and Marfurt, 2007;
135 Brown, 2011).

136 *Well data*

137 A slightly deviated exploration well (AT-8 #1 ST) was drilled in 1997 in the east of the study
138 area (Figure 2), encountering a c. 3600 m-thick, Pleistocene, deep-water clastic succession
139 (Figure 3). The well-log dataset includes gamma-ray (GR) and sonic (DT) data; we used these
140 logs to infer the lithology of the MTCs and their bounding strata via construction of a seismic-
141 to-well tie (Figure 6) (Wu et al., 2019). Five MTC-bearing intervals were drilled and logged by
142 AT-8 #1 ST. MTCs tend to have higher acoustic velocities and are more resistive than bounding
143 strata (i.e. pelagic/hemipelagic deposits, turbidites) at similar burial depths (Wu et al., 2019).
144 The MTCs are mudstone-rich, with the transported and remnant blocks they contain being
145 relatively sandstone-rich (Wu et al., 2019).

146 *Biostratigraphy data*

147 Plio-Pleistocene biostratigraphic data constrain the age of strata within, above, or below the
148 MTCs. Biostratigraphic data include planktonic foraminifera, and benthic regional and local
149 markers, along with regional and local calcareous nannoplankton markers spanning the late
150 Pliocene to Quaternary. Six biostratigraphic markers were identified by the contractors (see

151 Supplementary Material 1); we tied these to a biostratigraphic chart compiled for the Gulf of
152 Mexico (Witrock et al., 2003). The biostratigraphic framework is based on the last occurrence
153 or abundance acme of key biostratigraphic markers. These biostratigraphic data allow us to
154 provide a broad, temporal framework for the main tectono-sedimentary phases of minibasin
155 development, including the timing of MTC emplacement (see biostratigraphic data details in
156 caption of the Figure 3, see also Supplementary Material 1-2). We note that some
157 uncertainties exist when tying ages derived from biostratigraphic data, which are typically
158 obtained from borehole cuttings, to seismic reflection data, for which the vertical scale is
159 based on a conversion of two-way travel time to metres based on an understanding of
160 subsurface velocity variations. For example, Madof et al. (2009) indicate that the real depth
161 (in metres) of biostratigraphic datums could be higher or lower than the position of the
162 related horizons imaged and picked in seismic reflection data. In addition, mapping of age-
163 constrained seismic horizons away from the borehole AT-8 #1 ST across salt diapirs north and
164 south of Minibasin 5, and across salt-related normal faults (i.e., normal faults above salt diapir
165 E in Figure 3b), results in some uncertainties related to the local position of these horizons
166 within the minibasin fill.

167 Results

168 Seismic facies framework

169 Based on reflection amplitude (e.g. high versus low) and continuity (e.g. stratified versus
170 chaotic), we identify two main seismic facies in Minibasin 5 (Figure 5). Depositional elements
171 and processes are further interpreted based on lithology data provided by AT-8 #1 ST,
172 together with analogue information provided by seismic reflection- and well-based analysis
173 of similar depositional systems in adjacent areas (e.g., Prather et al., 1998; Posamentier and
174 Kolla, 2003; Roesink et al., 2004; Sincavage et al., 2004; Madof et al., 2009; Perov and
175 Bhattacharya, 2011; Madof et al., 2017; Wu et al., 2019). Stratified seismic facies are
176 characterised by good reflection continuity, and we further subdivide them based on
177 reflection amplitude and geometry (SFs1, SFs2 and SFs3; Figure 5). Overall, stratified seismic
178 facies document a range of non-MTC depositional elements (e.g. channels, lobes) deposited
179 by a range of processes (e.g. turbidity currents, suspension fallout). Chaotic seismic facies are
180 characterised by discontinuous, low- to medium-amplitude reflections, and we further

181 subdivide them based on their internal reflection pattern (SFc1, SFc2 and SFc3; Figure 5).
182 Overall, chaotic seismic facies record deposition within MTCs, emplaced by a range of MTC-
183 related processes (e.g. slumps, slides, debris flows). The seismic facies defined here form the
184 'building blocks' for the stratigraphic fill of Minibasin 5 (see below).

185 Stratigraphic framework of Minibasin 5

186 We identified seven seismic units in Minibasin 5, comprised of the two main seismic facies
187 (and inferred depositional elements) described above (Figure 6). Seismic unit 1 (SU-1) is c.
188 460-580 m thick, and consists of sandstone-rich channels and lobes, interbedded with
189 mudstone-rich slope deposits. Seismic unit 2 (SU-2) is c. 520-600 m thick, and comprises
190 sandstone-rich turbidite channel complexes and mudstone-rich slope deposits (Figure 6).
191 Seismic unit 3 (SU-3) is c. 530-640 m thick, and comprises sandstone- and mudstone-rich
192 MTCs, mudstone-rich slope sediments, and turbidite channel-fills (Figure 6). Seismic unit 4
193 (SU-4) is c. 210- 290 m thick and consists exclusively of mudstone-rich slope deposits. Seismic
194 unit 5 (SU-5) is c. 470-560 m thick, and consists mudstone-rich MTCs, sandstone-rich channel
195 complexes, and mudstone-rich slope deposits (Figure 6). Seismic unit 6 (SU-6) is c. 320-380 m
196 thick, and contains mudstone-rich slope deposits and sandstone-rich turbidite channel
197 complexes. The uppermost unit, Seismic unit 7 (SU-7), is c. 520-630 m thick, and consists of
198 sandstone- and mudstone-rich MTCs, mudstone-rich slope deposits, and sandstone-rich
199 turbidite channel complexes.

200 Tectono-stratigraphic development

201 We group the seven seismic units identified above into three age-constrained stages that
202 define the tectono-sedimentary development of Minibasin 5 (Figure 6). These stages are
203 defined by: (i) the geometrical characteristics of the main seismic packages (i.e. bowl- versus
204 wedge- versus layer-shaped; see Rowan & Weimer, 1999 and Jackson et al., 2019); (ii) the
205 way in which stratal units terminate against bounding salt diapirs, which we here describe
206 using the composite halokinetic sequence (CHS) terminological framework of Giles and
207 Rowan (2012); (iii) the types of depositional systems (e.g. channels, lobes, MTCs, etc.) they
208 contains; and (iv) changes in overall sediment accumulation rate derived from well and
209 biostratigraphic data.

210 Stage 1: Passive diapirism and minibasin downbuilding

211 *Description:*

212 Stage 1 consists of SU-1-3 and is early-middle Pleistocene. We identify two depocentres
213 during this stage (Figure 7a). The diapirs flanking these minibasins differ in that the western
214 one is relatively tall and has a steep margin, whereas the eastern one is of lower relief and
215 has a more gently dipping flank (Figure 4b, 8a). The minibasin fill during this stage is bowl-
216 shaped, with individual units progressively thinning towards and onlapping onto the flanking
217 diapirs (i.e. tapered CHSs of Giles and Rowan, 2012) (See figure 4b and 8a). Deposition of
218 slope channel-fills, lobes and slope sediments appear to characterise the early fill of this stage
219 (SU-1, SU-2), although at least two seismic-scale MTCs, encased in very fine-grained slope
220 deposits (SU-3), are identified in the upper part of the succession (Figure 6). The average
221 sediment accumulation rate during the deposition of SU-2 was c. 844 m/Myr (Figure 9).

222 *Interpretation:*

223 The presence of symmetrical, bowl-shaped packages indicates Minibasin 5 initially subsided
224 vertically and was flanked by passively rising diapirs during the early-middle Pleistocene. The
225 presence of tapered CHSs indicates sediment accumulation rate exceeded the diapir rise rate
226 at this time (Giles and Rowan, 2012). This high sediment accumulation rate may reflect a high
227 sediment supply rate, which may itself reflect the proximity of the study area to the
228 Mississippi River, which at this time delivered large volumes of sediment to upper slope
229 minibasins (Galloway et al., 2000; Galloway, 2001) (Figure 8a) .

230 **Stage 2: Load-driven passive salt diapirism**

231 *Description:*

232 Stage 2 comprises seismic units 4-6 and is middle-late Pleistocene. During this stage, the
233 northern depocentre shifts eastwards, whereas the southern depocentre simply expands
234 areally (Figure 7b). The western diapir is flanked by tabular (SU-4-6) CHSs, whereas the
235 eastern diapir is buried by the sediment (Figure 4b, 8b). The minibasin fill during this stage is
236 defined by broadly wedge-shaped package (See figure 3, 4, and 8b). Slope channel-fills are
237 deposited during the early part of this stage (SU-4), with an MTC, encased in slope mudstone
238 (SU-5), and ultimately, slope mudstone, intercalated with slope channel-fills (SU-6). The
239 average sediment accumulation rate increased to c. 1184 m/Myr during Stage 2 (Figure 9).

240 *Interpretation:*

241 During the middle-late Pleistocene, the paleo-Mississippi River continued to deliver
242 sediments to the upper slope minibasins (Figure 8b). The presence of wedge-shaped packages
243 records asymmetrical minibasin subsidence, and eastwards tilting of the northern minibasin
244 (Rowan and Weimer, 1998; Hudec et al., 2009; Jackson et al., 2019). The diapir flanking the
245 eastern side of minibasin was eventually covered by sediment, indicating an overall transition
246 to a time when sediment accumulation rate exceeded diapir rise rate. In contrast, the western
247 diapir continued to passively rise as the diapir rise rate exceeded sediment accumulation rate.
248 This interpretation is supported by the observation that tabular CHSs are deposited along this
249 diapir flank at this time (Figure 4b, 8b) (see Giles and Rowan, 2012).

250 Stage 3: Diapir burial, shortening, and active diapirism

251 *Description:*

252 Stage 3 comprises SU-7 and is late Pleistocene. During this stage, broadly layer-shaped
253 packages were deposited (See figure 3, 4, and 8c). Overall, this package gradually thins
254 towards yet extends across flanking salt diapirs, being thickest in the minibasin centre.
255 However, in detail, only the lower package (containing MTC-4) extends across the diapir, with
256 this being overlapped by an overlying package that is restricted to the minibasin centre. The
257 upper package extends across the diapir, showing only minimal thickness changes (See figure
258 4b and 8c). Fine-grained slope sediments, slope channel-fills, and two MTCs are deposited
259 during Stage 3. The average sediment accumulation rate at this time was the highest
260 documented during the post-early Pleistocene history of minibasin, reaching up to c. 10000
261 m/Myr (see Figure 9).

262 *Interpretation:*

263 During the late Pleistocene, large amounts of sediment continued to be delivered to the upper
264 slope and Minibasin 5 by the Mississippi River (Winker and Booth, 2000) (Figure 8c). The
265 thickness map indicates that much of the intra-slope accommodation formed by minibasin
266 subsidence was healed and that the flanking diapirs were buried (Figure 7c). The prevalence
267 of layer-like stratigraphic packages (i.e. which mainly record post-welding aggradation of
268 sediment above Minibasin 5 and its flanking diapirs) during Stage 3 reflects the high sediment

269 accumulation (and possibly supply) rate at this time. Rowan and Weimer (1998) also
270 interpreted that layer-shaped packages reflect relatively long-wavelength subsidence across
271 now-welded minibasins (see also the layer-shaped package from Jackson et al., 2019).

272 Characterisation of Minibasin 5 MTCs

273 MTC 1

274 *Description:*

275 MTC 1 (119 km² and 25 km³) is laterally and frontally confined by salt diapirs (Figure 10a, b).
276 It is 160-190 m thick, and its NW-SE-striking, south-western lateral margin defines a sharp
277 erosional contact between remobilised sediments (SFc3) and undeformed slope sediments
278 (SFs1 and SFs2) (Fig. 10c). The NW-SE-striking, north-eastern lateral margin of MTC 1 is
279 defined by the eastern salt diapir (Figure 10b). MTC 1 is sandstone-rich, containing large (130-
280 160 m thick), internally deformed, sandstone-rich (60-80% sandstone) blocks, intercalated
281 with thin mudstone layers (Wu et al., 2019). The highly reflective blocks, which have long axes
282 oriented NE-SW, are directly underlain by an interval of weakly reflective, more deformed
283 reflections (Figure 10d). NE-SW-striking, NW-dipping thrusts are observed within the blocks
284 (Figure 10b, c, d).

285 *Interpretation:*

286 Deformation at the base of the blocks suggests they were transported within MTC 1 (see for
287 example of transported blocks from Nardin et al., 1979; Bull et al., 2009a; Alves, 2015). The
288 orientation of the NE-SW-striking thrusts, and the NW-SE-striking lateral margins, suggest
289 that MTC 1 was transported towards the SE. We interpret the thrusts formed due to
290 horizontal compression of the debris flow adjacent to transported blocks. An alternative
291 interpretation is that the thrusts record shortening at the toe of the related mass movement.
292 The lithology of the large blocks suggests MTC 1 was derived from an up-dip, sand-rich source,
293 such as upper slope lobes and/or channels, and/or shelf-edge delta front deposits (Wu et al.,
294 2019). The sandstone-rich blocks may therefore have travelled c. 60 km from shelf-
295 edge/upper slope. Unfortunately, benthic foraminifera, which might help confirm the original
296 depositional setting, or at least water depth of these sandstones, are lacking. We suggest,
297 however, that blocks within MTC 1 are unlikely to have been derived from the nearby salt

298 diapirs because, at this time, the diapirs were capped by an intact sedimentary roof
299 comprising tapered CHS (see Figure 3 and 4).

300 MTC 2

301 *Description:*

302 MTC 2 (113.5 km² and 21.6 km³) is 110-150 m thick and has a similar external geometry to
303 MTC 1, being defined by: (i) a sharp, NW-SE-trending, erosional lateral margin on its south-
304 western side, and (ii) a NW-trending diapir on its north-eastern side (Figure 11a, b). MTC 2 is
305 mudstone-rich and contains subordinate, relatively sandstone-rich (30-40% sand) blocks that
306 are 20-40 m thick (Wu et al., 2019). In the centre of Minibasin 5, MTC 2 contains two large
307 (90-170 m) blocks, one of which contains mudstone-rich slope deposits at its base and
308 sandstone-rich Slope channel deposits at its top (Figure 11c) (Wu et al., 2019). The long axes
309 of these blocks trend NW (Figure 11b). Smaller blocks are clustered towards the north-east
310 minibasin margin (Figure 11a, b). Unlike the transported blocks in MTC 1, blocks in MTC 2
311 have sharp contacts with debritic material (SFc2), are not deformed, and are not underlain by
312 seismic-scale zones of deformation (Figure 11c).

313 *Interpretation:*

314 Based on the orientations of its lateral margins, we suggest MTC 2 was transported to the SE.
315 Although there is no direct evidence indicating the source area of MTC 2 (i.e. benthic
316 foraminifera), the presence of the subordinate sandstone-rich blocks, and similar kinematic
317 indicators to MTC 1 (i.e. the NW-SE-trending lateral margins), together suggest MTC 2 may
318 also have been derived from shelf-edge and/or upper slope. The seismic facies defining the
319 blocks (i.e. concordant, moderate-amplitude, continuous seismic reflections) are similar to
320 that of the underlying strata. The lack of deformation within these blocks implies they were
321 *not* transported, with the absence of deformation beneath them also suggesting the substrate
322 was *not* subjected to shear-induced deformation. Together, these two observations suggests
323 the blocks represent undeformed substrate material that was not transported within, but is
324 instead surrounded and capped by the MTC (i.e. 'remnant blocks'; (e.g. see examples of
325 remnant blocks from Frey Martinez et al., 2005; Lastras et al., 2005; Posamentier and Walker,
326 2006; Bull et al., 2009a; Gamboa et al., 2011)).

327 MTC 3 & 4

328 *Description:*

329 MTC 3 (123.5 km² and 20.3 km³) is 110-160 m thick and has a similar external geometry to
330 MTC 1 and 2, being bounded by: (i) a NW-trending trending erosional margin on its south-
331 western side, and (ii) NW-SE-striking diapir on its north-eastern side (Figure 12a, b). MTC 3 is
332 mudstone-dominated and contains sandstone-rich blocks (c. 20-40% sand) that are 30-60 m
333 thick (Wu et al., 2019). Biostratigraphic data indicate MTC 3 contains transported outer shelf
334 sediments (2377 m in well AT-8 #1 ST; Figure 13). Two biostratigraphic samples collected from
335 a slightly deeper position (2487 m), give an age of 0.78 and 0.83 Ma (lower Pleistocene; Figure
336 12c, 13, see details of the biostratigraphic samples from supplementary material 1).

337 MTC 4 (98.4 km² and 18.1 km³) has a similar geometry to the underlying MTCs, being again
338 defined by: (i) a NW-trending lateral margin on its south-western side, and (ii) NW-SE-striking
339 diapir on its north-eastern side (Figure 14a, b). MTC 4 is mudstone-rich and 70-110 m thick
340 (Figure 6), and contains remnant blocks, the long axes of which trend NW (Figure 14b).

341 *Interpretation:*

342 The orientations of their lateral margins suggest that MTC 3 and 4 were transported towards
343 the SE (e.g. Frey Martinez et al., 2005; Bull et al., 2009a). MTC 3 contains direct
344 biostratigraphic evidence that it was derived from the paleo shelf-edge (i.e. transported outer
345 shelf facies sample; Figure 13). The presence of two different age samples (0.78 and 0.85 Ma)
346 from the same depth (2478 m) within MTC 3 is intriguing. This might indicate that MTC 3,
347 emplaced at 0.78 Ma, entrained older (i.e. 0.83 Ma) substrate (i.e. seabed) material during
348 transport and emplacement (Figure 12d). An alternative interpretation is that the slightly old
349 (i.e. 0.83 Ma) material was shed from the roof of a growing diapir flanking the minibasin, and
350 reworked into the younger (i.e. 0.78 Ma) MTC 3 (Figure 12e). Because MTC 4 is similar to older
351 MTCs in terms of its geometry and kinematics, we infer it was also likely derived from the
352 upper slope or paleo shelf-edge.

353 **MTC 5**

354 *Description:*

355 MTC 5 (29.07 km² and 2.6 km³) is 110-180 m thick and was deposited in the centre of
356 Minibasin 5, being bounded by diapirs on its NE and W side, and a salt-cored structure high
357 on its SE side (Figure 15a, b). MTC 5 is sandstone-rich and is intercalated with thin mudstone

358 layers. Sandstone-rich blocks (c. 40-60% sand) that are 60-90 m thick occur within MTC 5. We
359 sub-divide MTC 5 into MTC 5.1 and MTC 5.2, based on cross-cutting relationships between
360 the lateral margins of the two units, with MTC 5.2 being slightly younger than MTC 5.1 (Figure
361 15b, d). MTC 5.1 is delineated by a set of NE-SW-striking normal faults and NE-SW-striking
362 thrusts in its proximal and distal parts, respectively (Figure 15b, 15c). MTC 5.2 has a NE-
363 trending headwall scarp, being bound by NW-SE-striking lateral margins. Well AT-8 #1 ST
364 intersected MTC 5.1, showing the deposit is sandstone-rich (Figure 6). However, well AT-8 #1
365 ST does not penetrate MTC 5.2, thus its lithology is unknown.

366 *Interpretation:*

367 The strike of the normal faults and thrusts suggest the bulk movement of MTC 5.1 was
368 towards the E (e.g. Frey Martinez et al., 2005; Bull et al., 2009a). The orientation of the
369 headwall scarp and lateral margins suggest that MTC 5.2 was transported to the SE (e.g. Bull
370 et al., 2009a). The confined nature of MTC 5.1 and 5.2 suggest they were both sourced from
371 locally positive topography generated by the growth of an underlying salt diapir.

372 **MTC 6**

373 *Description:*

374 MTC 6 (18.9 km² and 1.13 km³) is located just below the seabed along the south-eastern flank
375 of salt diapir A (Figure 16a, b). MTC 6 has well-defined, NW-trending lateral margins and is
376 50-70 m thick. In the up-dip part of MTC 6, N-S-striking normal faults occur on the flank of the
377 diapir, with hangingwall strata thickening towards and documenting syn-sedimentary growth
378 of the normal faults (Figure 16c). N-S-striking thrusts are also developed near the north-
379 eastern lateral margin of MTC 6; this margin is erosional, with the magnitude of erosion
380 increasing towards the northeast (Figure 16a, b). MTC 6 pinches-out to the southwest (Figure
381 16d). The N-S-striking normal faults and thrusts are present above the main body of MTC 6
382 (Fig. 16e). AT-8 #1 ST does not penetrate MTC 6, thus its lithology is unknown.

383 *Interpretation:*

384 The orientations of the normal faults and the lateral margins suggest MTC 6 was transported
385 to the SE. These spatial relationships suggest that MTC 6 was triggered by gravity-driven
386 instability of the seabed, driven by (relative) uplift of the seabed by diapir A. The
387 emplacement of MTC 6 created an exposed and unstable lateral margin along its NE side

388 (Figure 16d, 17 a). This margin thus collapsed, depositing material on top of the main body of
389 the MTC 6 (Figure 16e, 17b).

390 Discussion

391 Origin and classification of MTCs

392 Moscardelli and Wood (2008) classified MTCs as ‘attached’ (i.e. relatively far travelled, having
393 originated from the shelf-edge or upper slope) when the length: width ratio is >4 ; and
394 ‘detached’ (i.e. having originated from and being still partly physically connected to, a local
395 source, such as a salt-cored structural high) when the length: width ratio is <4 . Based on the
396 degree of internal deformation and morphology, Gamboa and Alves (2016) further classify
397 detached MTCs into Type 1 (i.e. highly deformed, with the length of the headwall: distance to
398 toe <1 , and with their long axes parallel to the transport direction) and Type 2 (i.e. less
399 deformed, with the length of the headwall: distance to toe >1 , and with their long axes
400 perpendicular to the transport direction). Because our data do not image their full extent, the
401 maximum length and width of the extrabasinal MTCs (MTC 1-4), the headwall length and
402 distance to toe length of intrabasinal MTC 5 remain unknown. Therefore, we cannot apply
403 the schemes of Moscardelli and Wood (2008) and Gamboa and Alves (2016), and instead use
404 morphometric and biostratigraphic data to classify our MTCs and to deduce if they were
405 derived locally or from beyond the minibasin. We here provide additional guidelines on how
406 to differentiate between attached and detached MTCs in salt-confined minibasin settings,
407 focusing on: (i) MTC morphometrics (i.e. external geometry, area, volume); (ii) the
408 composition and age of the MTCs; and (iii) the geometrical relationship between the MTCs
409 and bounding salt diapirs. We classify MTCs in such salt-influenced settings into: (i) shelf-
410 edge/upper slope derived MTCs and (ii) diapir-derived MTCs (Figure 18).

411 *Shelf-edge/upper slope derived MTCs (MTC 1-4)*

412 The shelf-edge-/upper slope-derived MTCs, sourced from the collapse of coeval shelf-edge
413 deltas, and/or supplied by reworked upper slope channels and lobes, tend to be, overall,
414 larger than the diapir-derived MTCs (i.e. 110-270 m thick; 113.5-123.5 km² in area; 20.3-25.1
415 km³ in volume). Shelf-edge-/upper slope-derived MTCs can be sandstone- or mudstone-rich,
416 and typically contain sandstone-rich blocks. Emplacement of these types MTC appear most
417 common during the initial phase of minibasin development, at a time when sediment

418 accumulation rate exceeded the rise rate of bounding passive diapirs (i.e. Stage 1 and 2; early
419 to middle Pleistocene) (Figure 19). In this salt-tectonic context, the lack of diapir-derived
420 MTCs is logical, given that at this time diapirs were unable to build sufficient differential relief
421 (i.e. topography) or steep slopes to trigger slope failure. The shelf-edge-/upper slope-derived
422 MTCs are thickest near the minibasin centre and were transported towards the SE, along a
423 bathymetric low laterally bound by salt diapirs; slope morphology controlled sediment
424 dispersal and ultimate preservation, even if it was not responsible for locally supplying
425 sediment. The trigger for slope failure and MTC emplacement is unknown.

426 The shelf-edge/upper slope-derived MTCs in Minibasin 5 are similar in terms of their location,
427 volume, and source area to so-called 'regional' or 'extra-basinal' MTCs described from other
428 minibasins (Madof et al., 2009; Doughty-Jones et al., 2019). More specifically, these MTCs: (i)
429 extend across the full width of the minibasin in which they are preserved, and occur in the
430 lowermost (i.e. earliest) part of the minibasin fill; (ii) are large in terms of their area and
431 volume when compared to diapir-derived or 'local' MTCs; and (iii) are sourced from the outer-
432 shelf and can contain outer-shelf bio-facies.

433 *Diapir-derived MTCs (MTC 5-6)*

434 Diapir-derived MTCs tend to be smaller than shelf-edge-/upper slope-derived MTCs (i.e. 50-
435 90 m thick; 18.9 to 29.7 km² in area; 1.13 to 2.6 km³ in volume). Diapir-derived MTCs were
436 emplaced during the latter stage of minibasin development, when the rate of diapir rise
437 appeared to have exceeded the rate of sediment accumulation (Stage 3; late Pleistocene)
438 (Figure 19). These MTCs are preserved on or immediately downdip of, the flanks of diapirs
439 (i.e. MTC 6), or on local topographic highs above buried diapirs (i.e. MTC 5). Diapir-derived
440 MTCs are thickest near diapir margins and thin downdip into the minibasin centres, indicating
441 local derivation from above or the flanks of diapir-cored structural highs. It is likely that the
442 preconditioning and triggering of this type of MTC is linked to localised gravitational instability,
443 more specifically oversteepening of diapir flanks during passive or active diapirism (discussed
444 below).

445 The diapir-derived MTCs in Minibasin 5 are comparable to so-called 'intra-basinal' or 'local'
446 MTCs described from other minibasins (Beaubouef et al., 2003; Owen et al., 2007; Madof et
447 al., 2009; Gamboa and Alves, 2016; Doughty-Jones et al., 2019). More specifically, these types
448 of MTC are: (i) preserved adjacent to the diapir from which they are sourced; (ii) are relatively

449 small in terms of their volume and areal extent; and (iii) developed in the uppermost (i.e.
450 latest) part of the minibasin fill, because at this time significant diapir-related structural relief
451 was developing around the minibasin margins.

452 Preconditioning factors and triggers for emplacement of minibasin-constrained 453 MTCs

454 *Eustasy*

455 Eustasy controls depositional processes and stratal patterns occurring in sedimentary basins
456 (e.g., Vail et al., 1977; Posamentier et al., 1988; Catuneanu, 2002; Posamentier and Kolla,
457 2003; Catuneanu et al., 2011). Eustasy was particularly important during the Pleistocene in
458 the northern Gulf of Mexico, when rapid (c. 500 years), high-amplitude (>100 m) sea-level
459 fluctuations resulted in rapid margin progradation and retrogradation (Galloway, 2001). For
460 example, Pleistocene sea level fluctuations are known to have caused major changes in the
461 position of the paleo-coastline (>100 km) during glacial intervals (Galloway et al., 2011).
462 During periods of sea-level fall, sediment supply was so high that deltas could reach the shelf-
463 edge. Rapid progradation during periods of sea-level fall and lowstand could increase pore-
464 fluid pressure within underlying, very fine-grained sediment, because these low intervals
465 could not efficiently expel their pore water when loaded by thick, shelf-edge deltas (Madof
466 et al., 2017). This primed or preconditioned the shelf-edge or upper slope to fail, or could
467 even trigger failure, resulting in the emplacement of shelf-edge/upper slope-derived MTCs
468 (Posamentier and Kolla, 2003). During periods of relatively rapid sea-level rise, transient
469 excess pore pressures could be generated in low-permeability sediment, decreasing slope
470 stability, and potentially triggering slope failure and the emplacement of upper slope-derived
471 MTCs (Smith et al., 2013).

472 There were numerous and frequent, glacio-eustatic sea-level fluctuations during the
473 Pleistocene in the Gulf of Mexico (Figure 20). It is thus be appealing to link MTC emplacement
474 to periods of falling and lowstands of sea level, via the causal mechanism outlined above.
475 However, we note there were many more sea-level falls and lowstands than there are
476 seismically resolvable MTCs in Minibasin 5. Any MTCs generated during periods of sea-level
477 fall may have: (i) been ponded in up-dip minibasins; (ii) transformed into turbidity currents
478 and bypassed Minibasin 5, being instead preserved in downdip minibasins; and (iii) been

479 emplaced in minibasins lateral to Minibasin 5. An alternative interpretation is that sea-level
480 variations and gravity-driven deep-water sedimentation are completely unrelated (Maslin et
481 al., 1998; Smith et al., 2013; Urlaub et al., 2013; Clare et al., 2014; Pope et al., 2015; Coussens
482 et al., 2016). In this case, other factors, such as sedimentation rate changes, fluid migration,
483 and salt diapirism, need to be considered.

484 *Sedimentation*

485 MTC emplacement may have been controlled by fluctuations in sediment supply; i.e. during
486 periods of high supply, which may have been climatically controlled, deltas may have reached
487 the shelf-edge even during highstands, before collapsing to supply MTCs. In the northern Gulf
488 of Mexico, Pleistocene sedimentation rates were extremely high, and more than double
489 Pliocene rates (Molnar, 2004). This increase reflects entrenchment and greater discharge of
490 the Mississippi River, related to its capture of the Ohio and Missouri rivers (Galloway et al.,
491 2011). The reorganisation of the Mississippi River System resulted in a significant sediment
492 supply increase and led to the development of submarine canyons that incised the shelf,
493 especially during periods of glacial retreat (Galloway et al., 2000; Rittenour et al., 2007;
494 Galloway et al., 2011; Bentley Sr et al., 2016). High sediment input from the Mississippi River
495 also caused rapid shelf-edge delta progradation; this could have increased delta-front
496 instability, and triggered sediment gravity currents (e.g., Sydow et al., 2003; Moscardelli et al.,
497 2006). We consider that the high sedimentation rates associated with paleo-Mississippi River
498 System were a key factor in preconditioning the shelf-edge/upper slope derived MTCs in the
499 study area.

500 *Geometric preconditioning (oversteepening)*

501 Minibasins are surrounded by diapirs that can rise and deform the overlying free surface. If
502 the related slope becomes sufficiently steep it can fail, triggering the emplacement of diapir-
503 derived MTCs (Cashman and Popenoe, 1985; Tripsanas et al., 2004; Madof et al., 2009; Hill et
504 al., 2011; Giles and Rowan, 2012). However, if the slope steepens relatively slowly, the
505 increase in steepness would take a long duration to pass a critical threshold and cause a
506 slope failure. In this case, the decomposition of gas hydrates or fluid migration (discussed
507 below) might accelerate the process, account for the preconditions and triggers of diapir
508 derived MTCs.

509 *Fluid migration*

510 The headwalls (i.e. where MTCs initiate, Bull et al., 2009a) of MTCs are most abundant on
511 slopes, in water depths of 1000-1500 m (or even deeper; e.g. Weaver et al., 2000; McHugh et
512 al., 2002; Hühnerbach and Masson, 2004), rather than close to the shelf-edge where the
513 sedimentation accumulation rates are highest. This suggests that sediment accumulation rate
514 (and perhaps related sea level fluctuations) are not the key control on the preconditioning
515 and triggering of upper-slope and minibasin-derived MTCs. Instead, fluid migration may play
516 an important role. More specifically, fluid could migrate to the upper slope along permeable
517 horizons that extend updip from the lower slope, with this sudden influx of fluids generating
518 excess pore pressure, thereby decreasing sediment shear strength and slope stability (Dugan
519 and Flemings, 2000; Masson et al., 2010).

520 *Gas hydrate dissociation*

521 Gas hydrates are common in shallowly buried (0-600 m below seabed) sediments in the
522 northern Gulf of Mexico (MacDonald et al., 1994; Milkov and Sassen, 2001; Boswell et al.,
523 2012). The dissociation of solid gas hydrate (the loss of free gas and water) may lead to rapid
524 sediment compaction and can generate excess pore pressures (Grozic, 2010). The process of
525 hydrate dissociation can also generate freshwater, which could play a role in leaching mud-
526 rich sediments, thereby increasing the quick clay behaviour of the mud-rich sediments (Bull
527 et al., 2009b). Gas hydrate dissociation could thus prime the slope to fail, and ultimately
528 trigger slope failure and MTC emplacement (e.g. the Storegga slide in Norway, Bryn et al.,
529 2005). Gas hydrates can be structurally focused above supra-salt faults that act as conduits
530 for the upward migration of deeply generated thermogenic gas into the shallower, gas
531 hydrate stability zone. As unstable gas hydrates normally occur 300-900 m below the seafloor
532 (Mienert et al., 2005), diapir-derived (in addition to shelf-edge/upper slope-derived) MTCs
533 could also be genetically related to the process of gas hydrate dissociation.

534 *Seismicity*

535 The study area is located along a relatively tectonically quiescent passive margin, in an area
536 generally regarded as having low overall seismicity (Franco et al., 2013). However, significant
537 seismic activity does locally and intermittently occur, with spatially variable peak ground
538 accelerations due to differential amplification and/or attenuation by the basin-fill. For
539 example, in 1978 a magnitude $M_w=5.0$ earthquake, triggered by an intraplate tectonic event,

540 occurred near central-northern Gulf of Mexico (Frohlich, 1982). A larger, magnitude $M_w=5.9$
541 event, which may have been triggered by the tectonic loading of the salt and its overburden,
542 took place in a nearby region in 2006 (Gangopadhyay and Sen, 2008). Smaller earthquakes
543 could also be triggered by increasing differential stresses related to the relatively high
544 sediment accumulation rates characterising the Pleistocene phase of Minibasin 5 (see
545 example from Lofoten and Norway Basins, Byrkjeland et al., 2000). Seismicity could therefore
546 trigger emplacement of the shelf-edge/upper slope- and diapir-derived MTCs encountered in
547 the study area.

548 The link between composite halokinetic sequences and MTCs

549 Halokinetic sequences are defined as “unconformity-bound packages of thinned and
550 deformed strata adjacent to passive diapirs” (Rowan et al., 2003). Halokinetic sequences
551 record cycles of passive and minor active diapirism, when salt periodically rises and pierces
552 the diapir roof (Rowan et al., 2003). Halokinetic sequences form as the rate of net vertical
553 diapiric rise varies relative to the local rate of sediment accumulation (Giles and Lawton, 2002;
554 Rowan et al., 2003). Within this conceptual framework, diapir-derived MTCs are most likely
555 to be emplaced in tabular composite halokinetic sequences, being generated by break-up of
556 the diapir roof, during a period when the diapir rise rate exceeds the sediment accumulation
557 rate (Giles and Rowan, 2012). Diapir-derived MTCs are thought to only extend a few hundred
558 metres away from their source diapirs (i.e. diapir-derived MTCs from Giles and Rowan, 2012;
559 Hearon et al., 2014).

560 Our observations are consistent with the outcrop--based model of Giles and Rowan (2012),
561 in that the intra-basinal MTCs (diapir-derived MTCs) are best-developed in Stage 3, when
562 tabular CHSs were deposited. However, we show that diapir-derived MTCs (i.e. MTC 6) can
563 extend significant distances (> 8 km) away from their source diapir. During the initial stage of
564 subsidence of Minibasin 5, when sediment accumulation rate exceeded diapir rise rate and
565 diapir-derived MTCs were accordingly absent, salt diapirs only provided the physical bounding
566 constraints for the distribution of extra-basinal MTCs (e.g. MTC 1 and 2); diapiric rise played
567 no role in triggering slope failure and MTC emplacement. Thus, during different stages of the
568 evolution of a minibasin, halokinetic sequences could have different relationships with their
569 associated MTCs.

570 Minibasin evolution; beyond the fill-and-spill model

571 The widely adopted fill-and-spill model has two key assumptions: (i) the longitudinal gradient
572 between two (or more) adjacent minibasins does not vary through time; and (ii)
573 sedimentation rate always exceeds the rate of minibasin subsidence (Beaubouef and
574 Friedmann, 2000; Booth et al., 2000; Booth et al., 2003). In fact, the fill-and-spill model
575 essentially views slope depocentres as being static.

576 Several studies show that the longitudinal gradients and the seabed bathymetry changes
577 through time because minibasins are dynamic not static, meaning the ratio of the rate of
578 accommodation creation to sediment supply/accumulation can be highly variable (e.g. Madof
579 et al., 2009; Sylvester et al., 2015; Madof et al., 2017). The original fill-and-spill model is thus
580 overly simplistic. Madof et al. (2017) propose a process-driven model of 'subsidence and
581 margin failure' for minibasin evolution; this better accounts for the seismic-stratigraphic
582 architecture of minibasins compared to the fill-and-spill model. In their model, rising diapirs
583 pond sediments within minibasins (Stage 1). The ponded sediments then promote minibasin
584 subsidence (due to density-driven downbuilding) and basin margin uplift (due to passive
585 diapirism) (Stage 2). Margin uplift leads to slope oversteepening, failure, and generation of
586 intra-basinal MTCs (Stage 3). Although this model is suitable for intra-basinal MTCs (i.e.
587 derived from salt minibasin margins), it does not address how extra-basinal, shelf-edge-
588 /upper slope-derived MTCs are emplaced in minibasins. Thus, we here extend their model by
589 taking halokinesis, subsidence and sedimentation into consideration, using our observations
590 from the northern Gulf of Mexico, in which MTCs constitute c. 60% of the minibasin fill.

591 We have identified three key stages during the evolution of Minibasin 5: (i) *Stage 1* – this
592 stage was characterised by relatively low sediment accumulation rates (c. 844 m/Myr) (Figure
593 20), passive diapirism, and broadly vertical subsidence of the minibasin; although sediment
594 accumulation rates were relatively low, they were high relative to the rise rate of the
595 bounding diapirs, resulting in the deposition of tapered CHSs. Sand-rich slope channel
596 complexes and lobes, as well as sand-rich, shelf-edge/upper slope-derived MTCs, were
597 deposited in the minibasin at this time (Figure 19). These extra-basinal MTCs were relatively
598 large (i.e. 25 km³) in relation to the minibasin size, and were deposited in the deepest, central
599 point of the minibasin. MTC emplacement was associated with substantial substrate
600 deformation; (ii) *Stage 2* – this stage was characterised by relatively high sedimentation rates

601 (c. 1184 m/Myr) (Figure 20), during which time the rise rate of passive diapirs exceeded the
602 sediment accumulation rate, resulting in the deposition of tabular CHSs. Mud-rich, shelf-edge-
603 derived MTCs (i.e. MTC 3), sand-rich slope-channel fills, and mud-rich slope deposits were
604 deposited during Stage 2 (Figure 19). Stage 2 MTCs are geometrically similar to Stage 1 MTCs,
605 but were smaller (i.e. 1.13km³); (iii) *Stage 3* - this final stage was characterised by very high
606 sediment accumulation rates (c. 10000 m/Myr) (Figure 20) that exceeded the rate of diapir
607 rise, resulting in capping of the minibasin-bounding diapirs by a relatively thick roof. Stage 3
608 saw deposition of sand-rich slope-channel fills and lobes, and sand-rich, diapir-derived MTCs
609 (Figure 19). These relatively small (i.e. 1.13km³), intra-basinal MTCs were sourced from and
610 deposited proximal to, the flanks of rising salt diapirs.

611 Our model develops the model of Madof et al. (2009), showing that: (i) the interplay between
612 the relative rate of salt diapir rise, minibasin subsidence, and sediment accumulation rate
613 dictates minibasin seismic-stratigraphic or stratigraphic architecture; (ii) MTCs are a key
614 stratigraphic element of marine minibasins; and (iii) the style of salt-related structural
615 deformation can be determined by the volume and type of coeval MTCs.

616 Conclusions

- 617 1. We use seismic reflection and well data to identify six MTCs in a Pleistocene, supra-
618 canopy minibasin in the northern Mississippi slope, northern Gulf of Mexico.
- 619 2. We identify two types of MTC that differ in their geometry, volume, and source area:
620 (i) relatively large (98.4-123 km² in area, 18.1-25 km³ in volume, 110-270 m in
621 thickness), shelf-edge/upper slope-derived, extra-basinal MTCs; (ii) relatively small
622 ((18.9-29.7 km² in area, 1.13-2.6 km³ in volume, 50-90 m in thickness), diapir-derived
623 MTCs, intra-basinal MTCs.
- 624 3. Shelf-edge/upper slope-derived MTCs were preferentially deposited during the earlier
625 phase of minibasin development when sediment accumulation rates exceeded diapir
626 rise rates. During this time, diapirs only constrained the distribution of shelf-
627 edge/upper slope-derived MTCs; they were not involved in the triggering of these
628 deposits. Diapir-derived MTCs were mainly deposited during the late stage of
629 minibasin development, at a time when salt diapir rise rate was lower than sediment
630 accumulation rate.

631 4. We present a model for minibasin development that highlights the role of MTCs and
632 develops the widely applied fill-and-spill model. More specifically, our models stresses:
633 (i) the interplay between the relative rate of salt diapir rise, minibasin subsidence, and
634 sediment accumulation rate dictates minibasin seismic-stratigraphic or stratigraphic
635 architecture; (ii) that MTCs are a key stratigraphic element of marine minibasins; and
636 (iii) the style of salt-related structural deformation can be determined by the volume
637 and type of coeval MTCs.

638 Figure Captions

639 Figure 1. Location map of the study area relative to the globe map (left) and the study area
640 (right), showing the position of the modern shelf-edge (black dotted line), paleo-shelf-edge
641 (white dotted line), and modern depositional systems. The location map is combined with
642 bathymetry (coloured) and northern Gulf Coastal Plain topography (blue and white) of the
643 Gulf of Mexico region. The study area (see yellow box) is located in the upper continental
644 slope of the northern Gulf of Mexico along the SW distal edge of the Mississippi Canyon. The
645 location of the Pleistocene-shelf edge is from Galloway et al. (2011), the Northern Gulf of
646 Mexico Deepwater Bathymetry map is modified from The Bureau of Ocean Energy
647 Management (BOEM).

648 Figure 2. Depth map (Depth below seabed) for top salt, showing the overall salt-tectonic
649 structure of the study area. 1-5 and A-C refer to minibasins and salt structures, respectively,
650 described in the text. See location from Figure 1.

651 Figure 3. (a) N-trending un-interpreted seismic section. (b) Interpreted N-trending seismic
652 section showing the overall salt-tectonic structure of the study area, the nine key seismic
653 horizons (H0 to seabed) and main MTC-bearing intervals (MTC 1 to MTC 6). See location from
654 figure 2. The biostratigraphic framework is based on the last occurrence or abundance acme
655 of key biostratigraphic markers. The details of the biostratigraphic data colorations are as
656 follows: the last occurrence of the early Pleistocene nannoplankton, *Scyphosphaera*
657 *pulcherima* (~1.92 Ma; Siesser, 1998; Young, 1998), correlates with our seismic horizon H0.

658 The abundance acme of the early Pleistocene planktonic foraminifera, *Sphaeroidinella*
659 *dehiscens acme B* (~1.62 Ma; Waterman et al., 2015), correlates with our seismic horizon H1.
660 The last occurrence of the early Pleistocene planktonic foraminifera, *Sphaeroidinella*
661 *dehiscens acme A* (~0.85 Ma; Waterman et al., 2015), correlates with our seismic horizon H3.
662 The last occurrence of the early Pleistocene calcareous nannoplankton, *Pseudoemiliana*
663 *lacunosa C* (~0.83 Ma; Waterman et al., 2015), correlates with our seismic horizon H5. The
664 last occurrence of the Late Pleistocene planktonic foraminifera, *Globorotalia flexuosa* (~0.07
665 Ma; Waterman et al., 2015), correlates with our seismic horizon H7.

666 Figure 4. (a) W-trending un-interpreted seismic section. (b) Interpreted W-trending seismic
667 section showing the overall salt-tectonic structure of the study area, the nine key seismic
668 horizons (H0 to seabed) and main MTC-bearing intervals (MTC 1 to MTC 5). See location from
669 Figure 2, and the details of the biostratigraphic data colorations from Figure 1 caption.

670 Figure 5. Main seismic facies summary, with seismic section of six seismic facies recognized in
671 the study area, a brief interpretation of the seismic facies, log facies, lithology, and facies
672 characteristics. See the text for detailed descriptions.

673 Figure 6. Correlation charts for the study area showing well logs (GR, Sonic, and ATR),
674 interpreted lithology, well correlated seismic section, key horizons, and geological age of each
675 episodes.

676 Figure 7. (a) Thickness map between horizon H0 and horizon H4, showing: (i) the thickness
677 variation of minibasin evolution stage 1; and (ii) the southern and northern depocentres
678 (labelled number 1 and 2). (b) Thickness map between horizon H4 and horizon H7, showing:
679 (i) the thickness variation of minibasin evolution stage 2; and (ii) the southern and northern
680 depocentres (labelled number 1 and 2). (c) Thickness map between horizon H7 and horizon
681 seabed, showing the thickness variation of minibasin evolution stage 3.

682 Figure 8. Cartoons of Minibasin 5 evolution model: (a) Passive diapirism and minibasin down-
683 building; (b) Load-driven passive salt diapirism; (c) Diapir burial, shortening, and active
684 diapirism.

685 Figure 9. Burial curve of Minibasin 5, the curve is plotted against the corresponding true
686 vertical depth. The horizontal axis representing the age and the vertical axis representing the

687 depth (sediment thickness), showing three stages of minibasin evolution. The average
688 sedimentation rates are estimated by the total thickness of the sediments deposited in each
689 stage divided by the time gap: (i) Stage 1 – c. 844 m/Myr; Stage 2 – c. 1184 m/Myr; Stage 3 –
690 c. 10000 m/Myr.

691 Figure 10. (a) Variance attribute calculated for the interval between the H2 and H2.1 seismic
692 horizons, showing the plain view of MTC 1; (b) Sketch of MTC 1 indicating key kinematic
693 features associated with MTC 1; (c) E-W oriented seismic section of MTC 1, see location from
694 Figure 10a; (d) NW-SE trending seismic section of MTC 1, see location from Figure 10a.

695 Figure 11 (a) Variance attribute calculated for the interval between the H3 and H4 seismic
696 horizons, showing the plain view of MTC 2; (b) Sketch of MTC 2 indicating key features
697 associated with this MTC; (c) SE-NW oriented seismic section of MTC 2, see location from
698 figure 11a.

699 Figure 12 (a) Chaos attribute calculated for the interval between the H5 and H5.1 seismic
700 horizons, showing the plain view of MTC 3; (b) Sketch of MTC 3 indicating key features
701 associated with this MTC; (c) SW-NE oriented seismic section of MTC 3, see location from
702 Figure 12a; (d) Sketch of MTC 3 showing that the origin of this MTC is from the shelf-edge; (e)
703 Sketch of MTC 3 showing that the emplacement process of MTC 3 is influenced by the uplift
704 of salt diapirs.

705 Figure 13. Biostratigraphy data compilation showing the age of six MTCs bearing intervals in
706 the study area.

707 Figure 14 (a) Variance attribute calculated for the interval between the H7.1 and H7.2 seismic
708 horizons, showing the map view of MTC 4; (b) Sketch of MTC 4 indicating key features
709 associated with this MTC.

710 Figure 15 (a) Variance attribute calculated for the interval between H7.3, H7.4 seismic
711 horizons, showing the map view of MTC 5; (b) Sketch of MTC 5 indicating key features
712 associated with this MTC; (c) NE-SW trending seismic section of MTC 5, see location from
713 Figure 15a; (d) SW-NW-NW trending seismic section of MTC 5, see location from Figure 15a.

714 Figure 16 (a) Variance attribute calculated for the interval between the H7.5 and H7.6 seismic
715 horizons, showing the map view of MTC 6; (b) Sketch of MTC 6 indicating key features

716 associated with this MTC; (c) SE-NW trending seismic section of MTC 6, see location from
717 Figure 16a; (d) SW-NE trending seismic section of MTC 6, see location from Figure 16a; (e) S-
718 N trending seismic section of MTC 6, see location from Figure 16a.

719 Figure 17 (a) Sketch of MTC 6 showing the first stage of the emplacement; (b) Sketch of MTC
720 6 showing the second stage of the emplacement.

721 Figure 18. Schematic 3D view of three different types of MTCs observed around the study
722 area: (i) Shelf-edge derived MTCs (SED); (ii) Upper slope derived MTCs (USD); and (iii) Diapir-
723 derived MTCs (DD).

724 Figure 19. Conceptual model for extrabasinal MTCs, intrabasinal MTCs, slope channels, and
725 background slope sediments.

726 Figure 20. Eustatic sea level curve for Pleistocene and Holocene correlated with general age
727 of the MTCs, modified from Imbrie et al. (1984); and the sedimentation rates curve through
728 time during different stage of minibasin evolution.

729 Reference

- 730 Alves, T. M., 2015, Submarine slide blocks and associated soft-sediment deformation in deep-water
731 basins: a review: *Marine and Petroleum Geology*, v. 67, p. 262-285.
- 732 Beaubouef, R., V. Abreu, J. Van Wagoner, H. Roberts, N. Rosen, R. Fillon, and J. Anderson, 2003,
733 Basin 4 of the Brazos–Trinity slope system, western Gulf of Mexico: the terminal portion of a
734 late Pleistocene lowstand systems tract: Shelf margin deltas and linked down slope
735 petroleum systems: Global significance and future exploration potential: *Proceedings of the*
736 *23rd Annual Research Conference, Gulf Coast Section SEPM Foundation*, p. 45-66.
- 737 Beaubouef, R., and S. Friedmann, 2000, High resolution seismic/sequence stratigraphic framework
738 for the evolution of Pleistocene intra slope basins, western Gulf of Mexico: depositional
739 models and reservoir analogs: *Deep-water reservoirs of the world: Gulf Coast Section SEPM*
740 *20th Annual Research Conference*, p. 40-60.
- 741 Bentley Sr, S., M. Blum, J. Maloney, L. Pond, and R. Paulsell, 2016, The Mississippi River source-to-
742 sink system: Perspectives on tectonic, climatic, and anthropogenic influences, Miocene to
743 Anthropocene: *Earth-Science Reviews*, v. 153, p. 139-174.
- 744 Booth, J., A. DuVernay III, D. Pfeiffer, and M. Styzen, 2000, Sequence stratigraphic framework,
745 depositional models, and stacking patterns of ponded and slope fan systems in the Auger
746 Basin: *Central Gulf of Mexico slope: Perkins Research Conference*, p. 82-103.
- 747 Booth, J. R., M. C. Dean, A. E. DuVernay III, and M. J. Styzen, 2003, Paleo-bathymetric controls on the
748 stratigraphic architecture and reservoir development of confined fans in the Auger Basin:
749 central Gulf of Mexico slope: *Marine and Petroleum Geology*, v. 20, p. 563-586.
- 750 Boswell, R., T. S. Collett, M. Frye, W. Shedd, D. R. McConnell, and D. Shelander, 2012, Subsurface gas
751 hydrates in the northern Gulf of Mexico: *Marine and Petroleum Geology*, v. 34, p. 4-30.
- 752 Brown, A. R., 2011, Interpretation of three-dimensional seismic data, *Society of Exploration*
753 *Geophysicists and American Association of Petroleum Geologists*.

754 Bryn, P., K. Berg, C. F. Forsberg, A. Solheim, and T. J. Kvalstad, 2005, Explaining the Storegga slide:
755 Marine and Petroleum Geology, v. 22, p. 11-19.

756 Bull, S., J. Cartwright, and M. Huuse, 2009a, A review of kinematic indicators from mass-transport
757 complexes using 3D seismic data: Marine and Petroleum Geology, v. 26, p. 1132-1151.

758 Bull, S., J. Cartwright, and M. Huuse, 2009b, A subsurface evacuation model for submarine slope
759 failure: Basin Research, v. 21, p. 433-443.

760 Byrkjeland, U., H. Bungum, and O. Eldholm, 2000, Seismotectonics of the Norwegian continental
761 margin: Journal of Geophysical Research: Solid Earth, v. 105, p. 6221-6236.

762 Canals, M., G. Lastras, R. Urgeles, J. Casamor, J. Mienert, A. Cattaneo, M. De Batist, H. Hafliðason, Y.
763 Imbo, and J. Laberg, 2004, Slope failure dynamics and impacts from seafloor and shallow
764 sub-seafloor geophysical data: case studies from the COSTA project: Marine Geology, v. 213,
765 p. 9-72.

766 Cashman, K., and P. Popenoe, 1985, Slumping and shallow faulting related to the presence of salt on
767 the continental slope and rise off North Carolina: Marine and Petroleum Geology, v. 2, p.
768 260-271.

769 Catuneanu, O., 2002, Sequence stratigraphy of clastic systems: concepts, merits, and pitfalls: Journal
770 of African Earth Sciences, v. 35, p. 1-43.

771 Catuneanu, O., W. E. Galloway, C. G. S. C. Kendall, A. D. Miall, H. W. Posamentier, A. Strasser, and M.
772 E. Tucker, 2011, Sequence stratigraphy: methodology and nomenclature: Newsletters on
773 stratigraphy, v. 44, p. 173-245.

774 Chopra, S., and K. J. Marfurt, 2007, Seismic attributes for prospect identification and reservoir
775 characterization, Society of Exploration Geophysicists and European Association of
776 Geoscientists and Engineers.

777 Clare, M. A., J. H. Clarke, P. J. Talling, M. J. Cartigny, and D. Pratomo, 2016, Preconditioning and
778 triggering of offshore slope failures and turbidity currents revealed by most detailed
779 monitoring yet at a fjord-head delta: Earth and Planetary Science Letters, v. 450, p. 208-220.

780 Clare, M. A., P. J. Talling, P. Challenor, G. Malgesini, and J. Hunt, 2014, Distal turbidites reveal a
781 common distribution for large (> 0.1 km³) submarine landslide recurrence: Geology, v. 42, p.
782 263-266.

783 Coussens, M., D. Wall - Palmer, P. J. Talling, S. F. Watt, M. Cassidy, M. Jutzeler, M. A. Clare, J. E.
784 Hunt, M. Manga, and T. M. Gernon, 2016, The relationship between eruptive activity, flank
785 collapse, and sea level at volcanic islands: A long - term (> 1 Ma) record offshore
786 Montserrat, Lesser Antilles: Geochemistry, Geophysics, Geosystems, v. 17, p. 2591-2611.

787 Diegel, F. A., J. Karlo, D. Schuster, R. Shoup, and P. Tauvers, 1995, Cenozoic structural evolution and
788 tectono-stratigraphic framework of the northern Gulf Coast continental margin.

789 Dott Jr, R., 1963, Dynamics of subaqueous gravity depositional processes: AAPG Bulletin, v. 47, p.
790 104-128.

791 Doughty-Jones, G., L. Lonergan, M. Mayall, and S. Dee, 2019, The role of structural growth in
792 controlling the facies and distribution of mass transport deposits in a deep-water salt
793 minibasin: Marine and Petroleum Geology, v. 104, p. 106-124.

794 Dugan, B., and P. B. Flemings, 2000, Overpressure and fluid flow in the New Jersey continental slope:
795 Implications for slope failure and cold seeps: Science, v. 289, p. 288-291.

796 Franco, S. I., C. Canet, A. Iglesias, and C. Valdés-González, 2013, Seismic activity in the Gulf of
797 Mexico. A preliminary analysis: Boletín de la Sociedad Geológica Mexicana, v. 65, p. 447-455.

798 Frey Martinez, J., J. Cartwright, and B. Hall, 2005, 3D seismic interpretation of slump complexes:
799 examples from the continental margin of Israel: Basin Research, v. 17, p. 83-108.

800 Frohlich, C., 1982, Seismicity of the central Gulf of Mexico: Geology, v. 10, p. 103-106.

801 Galloway, W. E., 2001, Cenozoic evolution of sediment accumulation in deltaic and shore-zone
802 depositional systems, northern Gulf of Mexico Basin: Marine and Petroleum Geology, v. 18,
803 p. 1031-1040.

804 Galloway, W. E., P. E. Ganey-Curry, X. Li, and R. T. Buffler, 2000, Cenozoic depositional history of the
805 Gulf of Mexico basin: AAPG bulletin, v. 84, p. 1743-1774.

806 Galloway, W. E., T. L. Whiteaker, and P. Ganey-Curry, 2011, History of Cenozoic North American
807 drainage basin evolution, sediment yield, and accumulation in the Gulf of Mexico basin:
808 Geosphere, v. 7, p. 938-973.

809 Gamboa, D., T. Alves, and J. Cartwright, 2011, Distribution and characterization of failed (mega)
810 blocks along salt ridges, southeast Brazil: Implications for vertical fluid flow on continental
811 margins: Journal of Geophysical Research: Solid Earth, v. 116.

812 Gamboa, D., and T. M. Alves, 2016, Bi-modal deformation styles in confined mass-transport deposits:
813 Examples from a salt minibasin in SE Brazil: Marine Geology, v. 379, p. 176-193.

814 Gangopadhyay, A., and M. K. Sen, 2008, A possible mechanism for the spatial distribution of
815 seismicity in northern Gulf of Mexico: Geophysical Journal International, v. 175, p. 1141-
816 1153.

817 Gee, M., D. Masson, A. Watts, and P. Allen, 1999, The Saharan debris flow: an insight into the
818 mechanics of long runout submarine debris flows: Sedimentology, v. 46, p. 317-335.

819 Giles, K. A., and T. F. Lawton, 2002, Halokinetic sequence stratigraphy adjacent to the El Papalote
820 diapir, northeastern Mexico: AAPG bulletin, v. 86, p. 823-840.

821 Giles, K. A., and M. G. Rowan, 2012, Concepts in halokinetic-sequence deformation and stratigraphy:
822 Geological Society, London, Special Publications, v. 363, p. 7-31.

823 Grozic, J., 2010, Interplay between gas hydrates and submarine slope failure, Submarine mass
824 movements and their consequences, Springer, p. 11-30.

825 Hampton, M. A., H. J. Lee, and J. Locat, 1996, Submarine landslides: Reviews of geophysics, v. 34, p.
826 33-59.

827 Harbitz, C. B., F. Løvholt, and H. Bungum, 2014, Submarine landslide tsunamis: how extreme and
828 how likely?: Natural Hazards, v. 72, p. 1341-1374.

829 Hearon, T. E., M. G. Rowan, K. A. Giles, and W. H. Hart, 2014, Halokinetic deformation adjacent to
830 the deepwater Auger diapir, Garden Banks 470, northern Gulf of Mexico: Testing the
831 applicability of an outcrop-based model using subsurface data: Interpretation, v. 2, p. SM57-
832 SM76.

833 Hill, A., J. Southgate, P. Fish, and S. Thomas, 2011, Deepwater Angola part I: Geohazard mitigation:
834 Frontiers in Offshore Geotechnics II, p. 209-214.

835 Hjelstuen, B. O., O. Eldholm, and J. I. Faleide, 2007, Recurrent Pleistocene mega-failures on the SW
836 Barents Sea margin: Earth and Planetary Science Letters, v. 258, p. 605-618.

837 Hudec, M. R., M. P. Jackson, and D. D. Schultz-Ela, 2009, The paradox of minibasin subsidence into
838 salt: Clues to the evolution of crustal basins: Geological Society of America Bulletin, v. 121, p.
839 201-221.

840 Hühnerbach, V., and D. Masson, 2004, Landslides in the North Atlantic and its adjacent seas: an
841 analysis of their morphology, setting and behaviour: Marine Geology, v. 213, p. 343-362.

842 Imbrie, J., J. D. Hays, D. G. Martinson, A. McIntyre, A. C. Mix, J. J. Morley, N. G. Pisias, W. L. Prell, and
843 N. J. Shackleton, 1984, The orbital theory of Pleistocene climate: support from a revised
844 chronology of the marine $\delta^{18}O$ record.

845 Jackson, C. A.-L., O. B. Duffy, N. Fernandez, T. Dooley, M. Hudec, M. Jackson, and G. Burg, 2019, The
846 Stratigraphic Record of Minibasin Subsidence.

847 Kioka, A., T. Schwestermann, J. Moernaut, K. Ikehara, T. Kanamatsu, C. McHugh, C. dos Santos
848 Ferreira, G. Wiemer, N. Haghipour, and A. Kopf, 2019, Megathrust earthquake drives drastic
849 organic carbon supply to the hadal trench: Scientific reports, v. 9, p. 1553.

850 Kneller, E. A., and C. A. Johnson, 2011, Plate kinematics of the Gulf of Mexico based on integrated
851 observations from the Central and South Atlantic.

852 Kvalstad, T. J., L. Andresen, C. F. Forsberg, K. Berg, P. Bryn, and M. Wangen, 2005, The Storegga slide:
853 evaluation of triggering sources and slide mechanics: Marine and Petroleum Geology, v. 22,
854 p. 245-256.

855 Lastras, G., F. V. De Blasio, M. Canals, and A. Elverhøi, 2005, Conceptual and numerical modeling of
856 the BIG'95 debris flow, western Mediterranean Sea: *Journal of Sedimentary Research*, v. 75,
857 p. 784-797.

858 Li, W., T. M. Alves, S. Wu, D. Völker, F. Zhao, L. Mi, and A. Kopf, 2015, Recurrent slope failure and
859 submarine channel incision as key factors controlling reservoir potential in the South China
860 Sea (Qiongdongnan Basin, South Hainan Island): *Marine and Petroleum Geology*, v. 64, p. 17-
861 30.

862 Locat, J., and H. J. Lee, 2002, Submarine landslides: advances and challenges: *Canadian Geotechnical*
863 *Journal*, v. 39, p. 193-212.

864 MacDonald, I., N. Guinasso Jr, R. Sassen, J. Brooks, L. Lee, and K. Scott, 1994, Gas hydrate that
865 breaches the sea floor on the continental slope of the Gulf of Mexico: *Geology*, v. 22, p. 699-
866 702.

867 Madof, A. S., N. Christie-Blick, and M. H. Anders, 2009, Stratigraphic controls on a salt-withdrawal
868 intraslope minibasin, north-central Green Canyon, Gulf of Mexico: Implications for
869 misinterpreting sea level change: *AAPG bulletin*, v. 93, p. 535-561.

870 Madof, A. S., N. Christie-Blick, M. H. Anders, and L. A. Febo, 2017, Unreciprocated sedimentation
871 along a mud-dominated continental margin, Gulf of Mexico, USA: Implications for sequence
872 stratigraphy in muddy settings devoid of depositional sequences: *Marine and Petroleum*
873 *Geology*, v. 80, p. 492-516.

874 Mallarino, G., R. T. Beaubouef, A. W. Droxler, V. Abreu, and L. Labeyrie, 2006, Sea level influence on
875 the nature and timing of a minibasin sedimentary fill (northwestern slope of the Gulf of
876 Mexico): *AAPG bulletin*, v. 90, p. 1089-1119.

877 Maslin, M., N. Mikkelsen, C. Vilela, and B. Haq, 1998, Sea-level–and gas-hydrate–controlled
878 catastrophic sediment failures of the Amazon Fan: *Geology*, v. 26, p. 1107-1110.

879 Masson, D., C. Harbitz, R. Wynn, G. Pedersen, and F. Løvholt, 2006, Submarine landslides: processes,
880 triggers and hazard prediction: *Philosophical Transactions of the Royal Society A:*
881 *Mathematical, Physical and Engineering Sciences*, v. 364, p. 2009-2039.

882 Masson, D., R. Wynn, and P. Talling, 2010, Large landslides on passive continental margins:
883 processes, hypotheses and outstanding questions, *Submarine mass movements and their*
884 *consequences*, Springer, p. 153-165.

885 McHugh, C. M., J. E. Damuth, and G. S. Mountain, 2002, Cenozoic mass-transport facies and their
886 correlation with relative sea-level change, New Jersey continental margin: *Marine Geology*,
887 v. 184, p. 295-334.

888 Mienert, J., M. Vanneste, S. Bünz, K. Andreassen, H. Haflidason, and H. P. Sejrup, 2005, Ocean
889 warming and gas hydrate stability on the mid-Norwegian margin at the Storegga Slide:
890 *Marine and Petroleum Geology*, v. 22, p. 233-244.

891 Milkov, A. V., and R. Sassen, 2001, Estimate of gas hydrate resource, northwestern Gulf of Mexico
892 continental slope: *Marine Geology*, v. 179, p. 71-83.

893 Molnar, P., 2004, Late Cenozoic increase in accumulation rates of terrestrial sediment: How might
894 climate change have affected erosion rates?: *Annu. Rev. Earth Planet. Sci.*, v. 32, p. 67-89.

895 Moscardelli, L., and L. Wood, 2008, New classification system for mass transport complexes in
896 offshore Trinidad: *Basin Research*, v. 20, p. 73-98.

897 Moscardelli, L., L. Wood, and P. Mann, 2006, Mass-transport complexes and associated processes in
898 the offshore area of Trinidad and Venezuela: *AAPG bulletin*, v. 90, p. 1059-1088.

899 Nardin, T. R., F. Hein, D. S. Gorsline, and B. Edwards, 1979, A review of mass movement processes
900 sediment and acoustic characteristics, and contrasts in slope and base-of-slope systems
901 versus canyon-fan-basin floor systems.

902 Nisbet, E. G., and D. J. Piper, 1998, Giant submarine landslides: *Nature*, v. 392, p. 329-330.

903 O'loughlin, K. F., and J. F. Lander, 2003, *Caribbean tsunamis: a 500-year history from 1498-1998*, v.
904 20, Springer Science & Business Media.

905 Omosanya, K. O., and T. M. Alves, 2013, A 3-dimensional seismic method to assess the provenance
906 of Mass-Transport Deposits (MTDs) on salt-rich continental slopes (Espírito Santo Basin, SE
907 Brazil): *Marine and Petroleum Geology*, v. 44, p. 223-239.

908 Ortiz - Karpf, A., D. M. Hodgson, C. A. L. Jackson, and W. D. McCaffrey, 2016, Mass - Transport
909 Complexes as Markers of Deep - Water Fold - and - Thrust Belt Evolution: Insights from the
910 Southern Magdalena Fan, Offshore Colombia: *Basin Research*.

911 Owen, M., S. Day, and M. Maslin, 2007, Late Pleistocene submarine mass movements: occurrence
912 and causes: *Quaternary Science Reviews*, v. 26, p. 958-978.

913 Perov, G., and J. P. Bhattacharya, 2011, Pleistocene shelf-margin delta: Intradeltaic deformation and
914 sediment bypass, northern Gulf of Mexico: *AAPG bulletin*, v. 95, p. 1617-1641.

915 Pindell, J., and J. F. Dewey, 1982, Permo - Triassic reconstruction of western Pangea and the
916 evolution of the Gulf of Mexico/Caribbean region: *Tectonics*, v. 1, p. 179-211.

917 Pope, E., P. Talling, M. Urlaub, J. Hunt, M. Clare, and P. Challenor, 2015, Are large submarine
918 landslides temporally random or do uncertainties in available age constraints make it
919 impossible to tell?: *Marine Geology*, v. 369, p. 19-33.

920 Posamentier, H., M. Jervey, and P. Vail, 1988, Eustatic controls on clastic deposition I—conceptual
921 framework.

922 Posamentier, H., and R. Walker, 2006, Deep-water turbidites and submarine fans. *Facies Models*
923 *Revisited: Special Publication-Society for Sedimentary Geology*, v. 84, p. 399-520.

924 Posamentier, H. W., and V. Kolla, 2003, Seismic geomorphology and stratigraphy of depositional
925 elements in deep-water settings: *Journal of Sedimentary Research*, v. 73, p. 367-388.

926 Prather, B., 2000, Calibration and visualization of depositional process models for above-grade
927 slopes: a case study from the Gulf of Mexico: *Marine and Petroleum Geology*, v. 17, p. 619-
928 638.

929 Prather, B. E., J. R. Booth, G. S. Steffens, and P. A. Craig, 1998, Classification, lithologic calibration,
930 and stratigraphic succession of seismic facies of intraslope basins, deep-water Gulf of
931 Mexico: *AAPG bulletin*, v. 82, p. 701-728.

932 Prather, B. E., C. Pirmez, C. D. Winker, M. Deptuck, and D. Mohrig, 2012, Stratigraphy of linked
933 intraslope basins: Brazos-Trinity system western Gulf of Mexico: Application of the principles
934 of seismic geomorphology to continental-slope and base-of-slope systems: Case studies
935 from seafloor and near-seafloor analogues: *SEPM, Special Publication*, v. 99, p. 83-109.

936 Rittenour, T. M., M. D. Blum, and R. J. Goble, 2007, Fluvial evolution of the lower Mississippi River
937 valley during the last 100 ky glacial cycle: Response to glaciation and sea-level change: *GSA*
938 *Bulletin*, v. 119, p. 586-608.

939 Roesink, J. G., P. Weimer, and R. Bouroullec, 2004, Sequence stratigraphy of Miocene to Pleistocene
940 sediments of east-central Mississippi canyon, northern Gulf of Mexico.

941 Rowan, M. G., T. F. Lawton, K. A. Giles, and R. A. Ratliff, 2003, Near-salt deformation in La Popa
942 basin, Mexico, and the northern Gulf of Mexico: A general model for passive diapirism: *AAPG*
943 *bulletin*, v. 87, p. 733-756.

944 Rowan, M. G., and P. Weimer, 1998, Salt-sediment interaction, northern Green Canyon and Ewing
945 bank (offshore Louisiana), northern Gulf of Mexico: *AAPG bulletin*, v. 82, p. 1055-1082.

946 Salazar, J. A., J. H. Knapp, C. C. Knapp, and D. R. Pyles, 2014, Salt tectonics and Pliocene stratigraphic
947 framework at MC-118, Gulf of Mexico: An integrated approach with application to deep-
948 water confined structures in salt basins: *Marine and Petroleum Geology*, v. 50, p. 51-67.

949 Salvador, A., 1987, Late Triassic-Jurassic paleogeography and origin of Gulf of Mexico basin: *AAPG*
950 *Bulletin*, v. 71, p. 419-451.

951 Sawyer, D. E., P. B. Flemings, B. Dugan, and J. T. Germaine, 2009, Retrogressive failures recorded in
952 mass transport deposits in the Ursa Basin, Northern Gulf of Mexico: *Journal of Geophysical*
953 *Research: Solid Earth*, v. 114.

954 Sawyer, D. E., P. B. Flemings, R. C. Shipp, and C. D. Winker, 2007, Seismic geomorphology, lithology,
955 and evolution of the late Pleistocene Mars-Ursa turbidite region, Mississippi Canyon area,
956 northern Gulf of Mexico: AAPG bulletin, v. 91, p. 215-234.

957 Shipp, R. C., 2004, Physical Characteristics and Impact of Mass Transport Complexes on Deepwater
958 Jetted Conductors and Suction Anchor Piles.

959 Siesser, W. G., 1998, Calcareous nannofossil genus *Scyphosphaera*: structure, taxonomy,
960 biostratigraphy, and phylogeny: *Micropaleontology*, p. 351-384.

961 Sincavage, R., P. Weimer, and R. Bouroullec, 2004, Sequence Stratigraphy of Upper-Miocene to
962 Pleistocene Sediments of Southwestern Mississippi Canyon and Northwestern Atwater
963 Valley, Northern Gulf of Mexico.

964 Smith, D., S. Harrison, and J. T. Jordan, 2013, Sea level rise and submarine mass failures on open
965 continental margins: *Quaternary Science Reviews*, v. 82, p. 93-103.

966 Strout, J. M., and T. I. Tjelta, 2005, In situ pore pressures: What is their significance and how can they
967 be reliably measured?: *Marine and Petroleum Geology*, v. 22, p. 275-285.

968 Sydow, J., J. Finneran, A. P. Bowman, H. Roberts, N. Rosen, R. Fillon, and J. Anderson, 2003, Stacked
969 shelf-edge delta reservoirs of the Columbus Basin, Trinidad, West Indies: *Shelf-Margin Deltas
970 and Linked Downslope Petroleum Systems*, p. 441-465.

971 Sylvester, Z., A. Cantelli, and C. Pirmez, 2015, Stratigraphic evolution of intraslope minibasins:
972 Insights from surface-based model: *AAPG Bulletin*, v. 99, p. 1099-1129.

973 Talling, P. J., L. A. Amy, and R. B. Wynn, 2007, New insight into the evolution of large - volume
974 turbidity currents: comparison of turbidite shape and previous modelling results:
975 *Sedimentology*, v. 54, p. 737-769.

976 Talling, P. J., M. L. CLARE, M. Urlaub, E. Pope, J. E. Hunt, and S. F. Watt, 2014, Large submarine
977 landslides on continental slopes: geohazards, methane release, and climate change:
978 *Oceanography*, v. 27, p. 32-45.

979 Tripsanas, E. K., W. R. Bryant, and B. A. Phaneuf, 2004, Slope-instability processes caused by salt
980 movements in a complex deep-water environment, Bryant Canyon area, northwest Gulf of
981 Mexico: *AAPG bulletin*, v. 88, p. 801-823.

982 Twichell, D. C., J. D. Chaytor, S. Uri, and B. Buczkowski, 2009, Morphology of late Quaternary
983 submarine landslides along the US Atlantic continental margin: *Marine Geology*, v. 264, p. 4-
984 15.

985 Urlaub, M., P. J. Talling, and D. G. Masson, 2013, Timing and frequency of large submarine
986 landslides: implications for understanding triggers and future geohazard: *Quaternary Science
987 Reviews*, v. 72, p. 63-82.

988 Vail, P. R., R. Mitchum Jr, and S. Thompson III, 1977, *Seismic Stratigraphy and Global Changes of Sea
989 Level: Part 4. Global Cycles of Relative Changes of Sea Level.: Section 2. Application of
990 Seismic Reflection Configuration to Stratigraphic Interpretation.*

991 Waterman, A., R. Weber, B. Brace, J. Edmunds, R. Fillon, R. George, Y. Lu, N. Myers, B. Parker, and T.
992 Reilly, 2015, *Biostratigraphic chart—Gulf Basin, USA: Quaternary and Neogene.*

993 Weaver, P. P., R. B. Wynn, N. H. Kenyon, and J. Evans, 2000, Continental margin sedimentation, with
994 special reference to the north - east Atlantic margin: *Sedimentology*, v. 47, p. 239-256.

995 Weimer, P., and C. Shipp, 2004, Mass transport complex: musing on past uses and suggestions for
996 future directions: *Offshore Technology Conference.*

997 Winker, C. D., and J. R. Booth, 2000, Sedimentary dynamics of the salt-dominated continental slope,
998 Gulf of Mexico: integration of observations from the seafloor, near-surface, and deep
999 subsurface: *GCSSEPM Foundation 20th Annual Research Conference, Deep-Water Reservoirs
1000 of the World*, p. 1059-1086.

1001 Witrock, R., A. Friedmann, J. Galluzzo, L. Nixon, P. Post, and K. Ross, 2003, *Biostratigraphic chart of
1002 the Gulf of Mexico offshore region: Jurassic to Quaternary, US Department of the Interior,
1003 Minerals Management Service, New Orleans.*

1004 Wu, N., C. A. Jackson, H. Johnson, and D. M. Hodgson, 2019, Lithological, petrophysical and seal
1005 properties of mass-transport complexes (MTCs), northern Gulf of Mexico: EarthArXiv.
1006 February, v. 19.

1007 Yeakley, J. A., A. Shakoor, and W. Johnson, 2019, Influence of Salt Tectonics On Fault Displacements
1008 and Submarine Slope Failures from Algeria To Sardinia: Environmental & Engineering
1009 Geoscience, p. 1-13.

1010 Young, J. R., 1998, Neogene: Calcareous nannofossil biostratigraphy, p. 225-265.

1011

1012

Figure 1

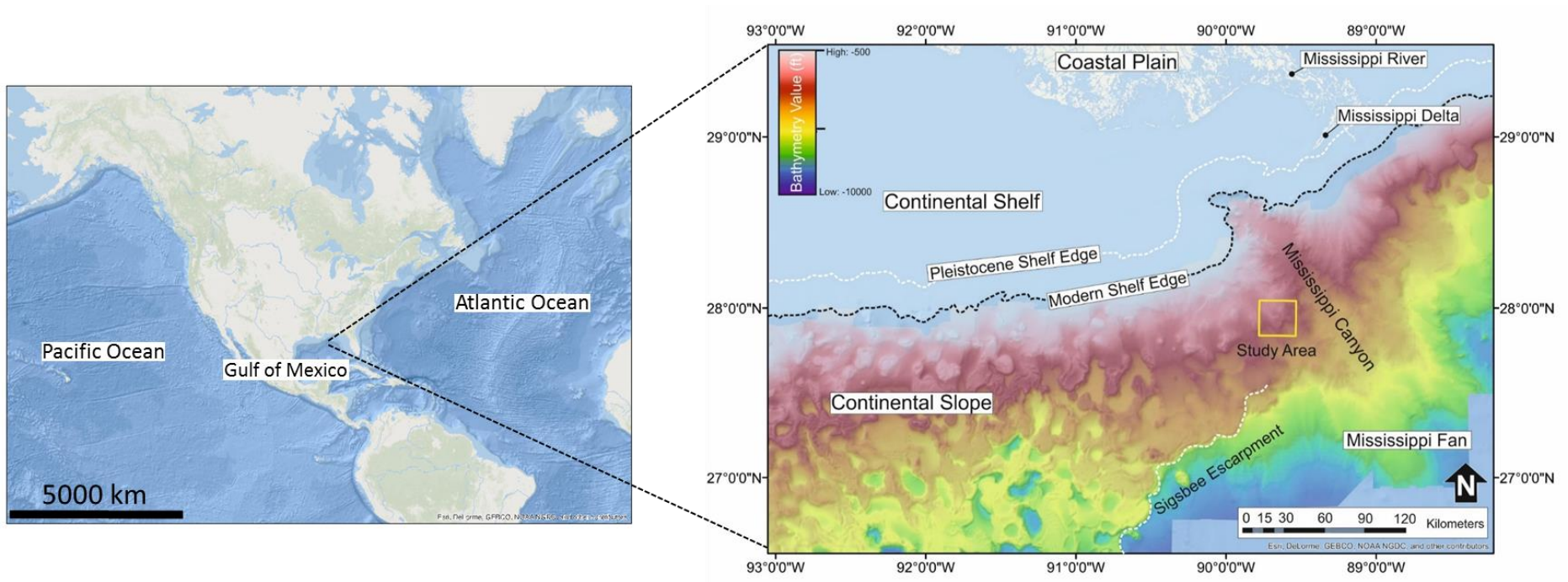


Figure 2

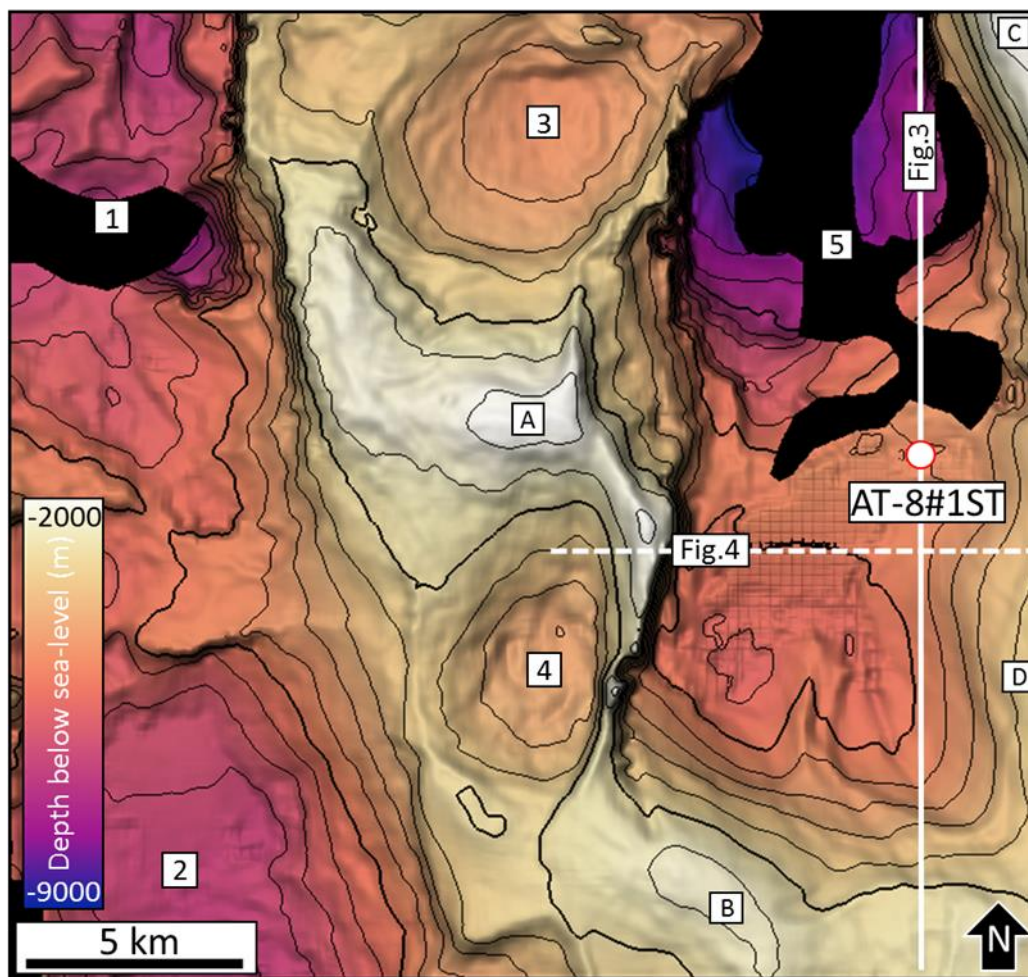


Figure 3a

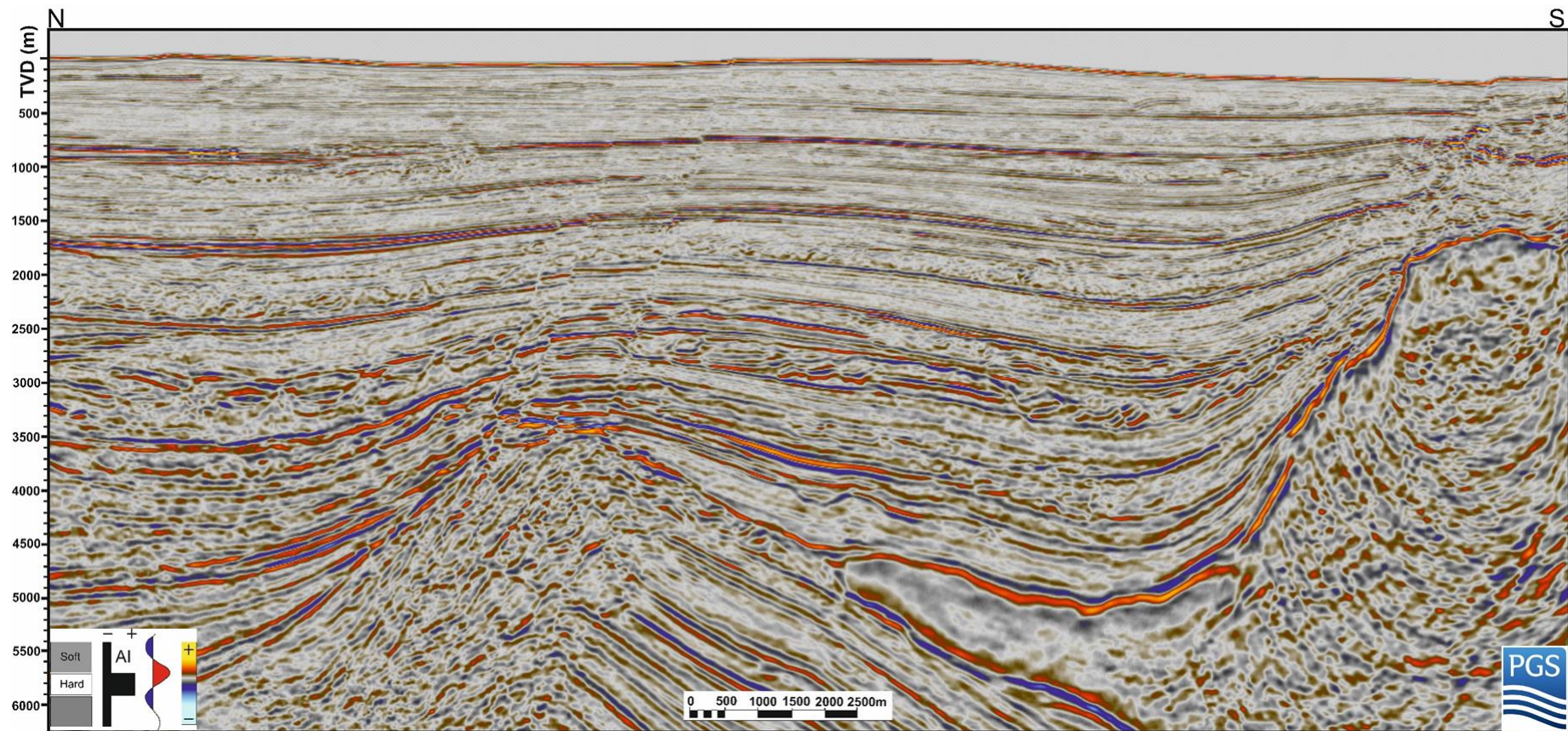


Figure 3b

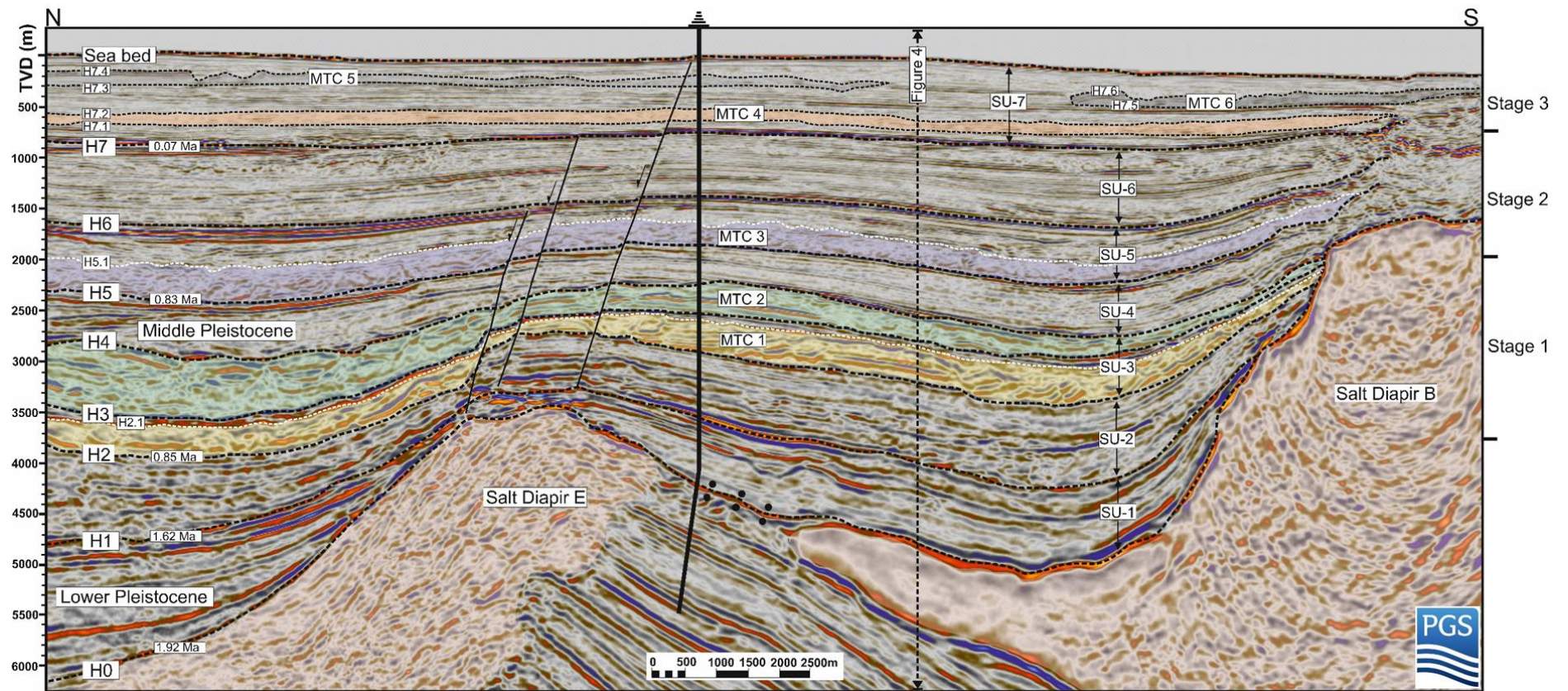


Figure 4a

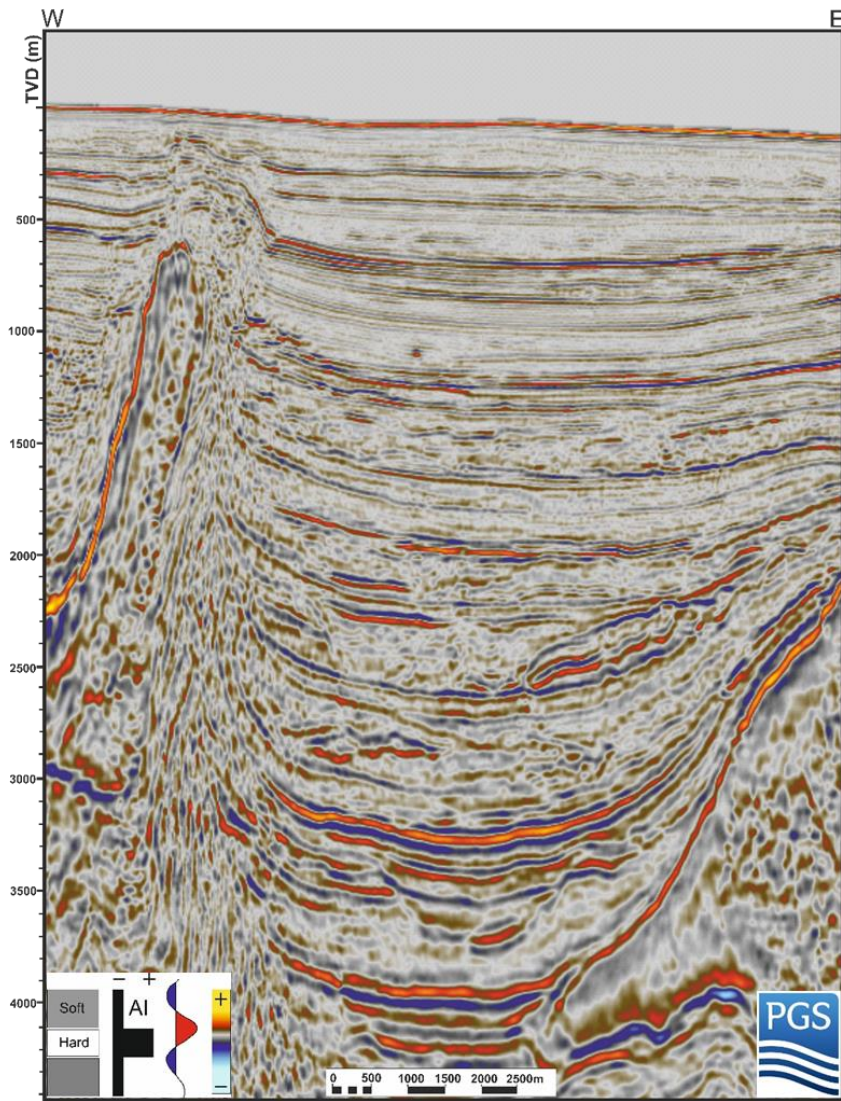


Figure 4b

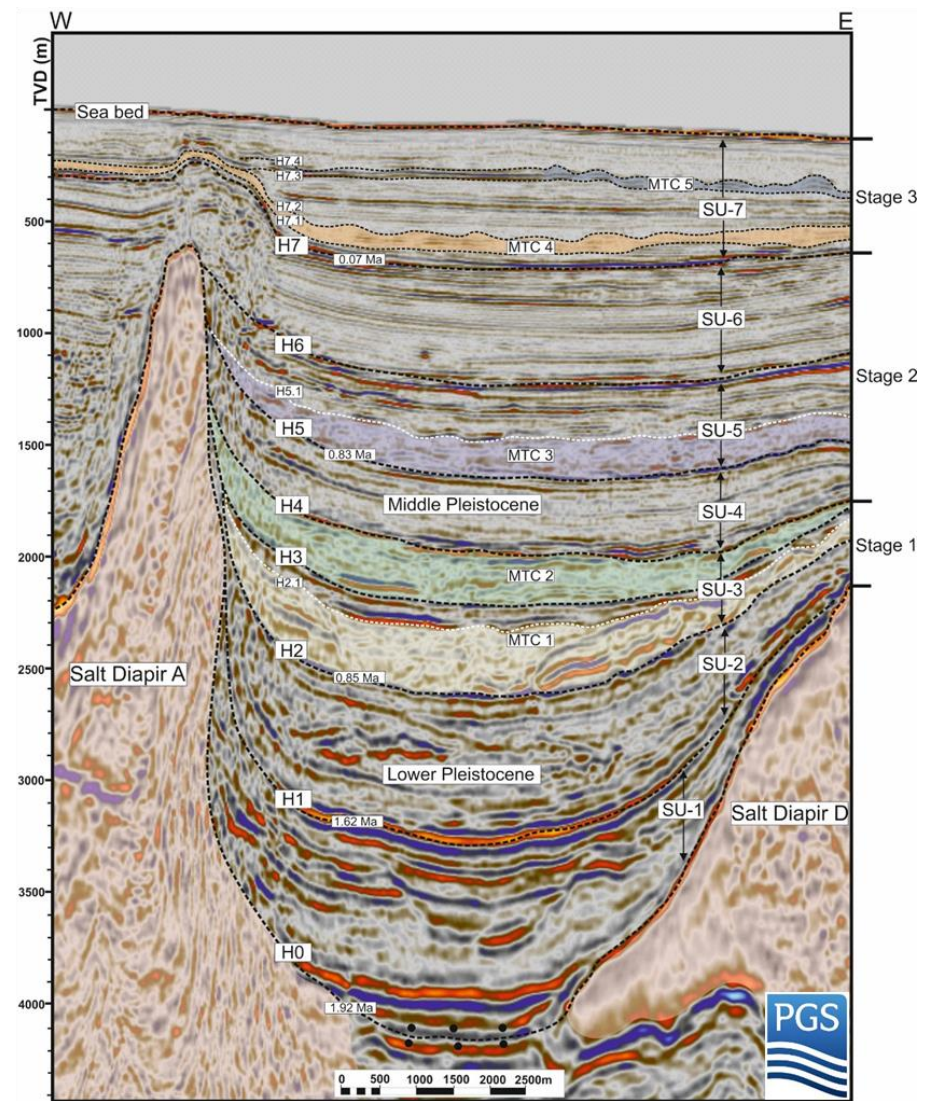


Figure 5

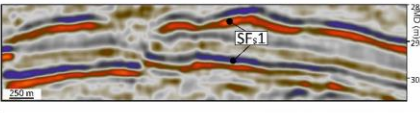


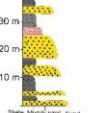
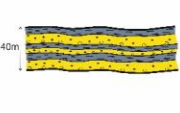
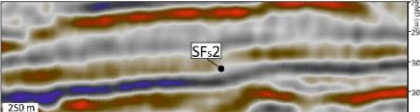


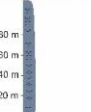
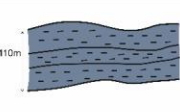
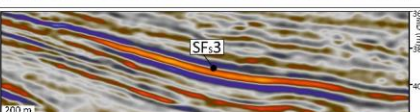


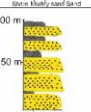
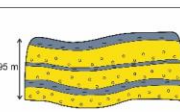
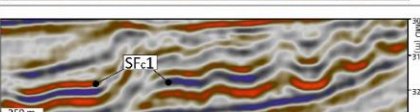


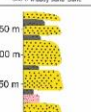
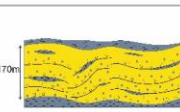
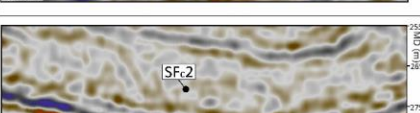


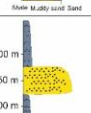
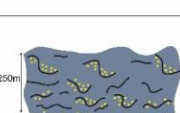
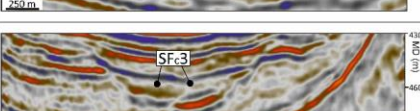


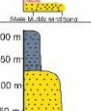
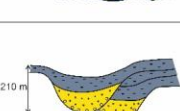
Seismic facies template										
Types	Seismic sections	GR	Sonic	Lithology	Schematic facies geometries	Seismic facies	Log facies	Lithology	Depositional element	
Stratified facies	SF _{s1}						Fair continuity, parallel, high amplitude seismic reflections, with slightly inclined, non-erosive planar base and top surface.	Fining upward trend with low GR response at the base and high GR response at the top.	Sandstone rich at the bottom and grading upward into mudstone rich deposits at the top.	Heterogeneous gravity flow deposit: • Levees • Lobes • Channel systems.
	SF _{s2}						Fair continuity, parallel, low to medium amplitude seismic reflections, with flat base and top surfaces.	Constantly serrated high GR response from bottom to top.	Mudstone rich deposits from base to top.	Slope.
	SF _{s3}						• Fair continuity, high amplitude seismic reflections, with non-erosive, oblique top and base surfaces.	• Box-shaped GR response at base and middle, bell-shaped with upward fining GR response at the top.	Sandstone rich deposit dominant interbedded with mudstone deposits.	Lobes.
Chaotic facies	SF _{c1}						Locally disorganised, faulted and folded, high amplitude seismic reflections, with a tabular external form.	Bell-shaped GR response with a fining upward trend near the bottom, and a set of box-shaped low GR response at middle and top.	Mudstone-rich deposit at the bottom, sandstone-rich deposits interbedded with thinly bedded mudstone at the middle and upper parts.	MTCs containing large sandstone-rich blocks.
	SF _{c2}						Mixture of low to medium amplitude seismic reflections with highly chaotic internal reflection pattern.	Serrated, overall high GR response that locally contains sharp-based, box-shaped, low GR intervals from base to top.	Mudstone-rich deposit interbedded with sandstone rich blocks.	Mudstone dominated MTCs Subordinate sandstones blocks (30-60 m).
	SF _{c3}						Chaotic, medium-high amplitude seismic reflections, 'bowl' shaped external form with an erosional base.		Sandstone rich deposits.	Sandstone dominant slope channel.

Figure 6

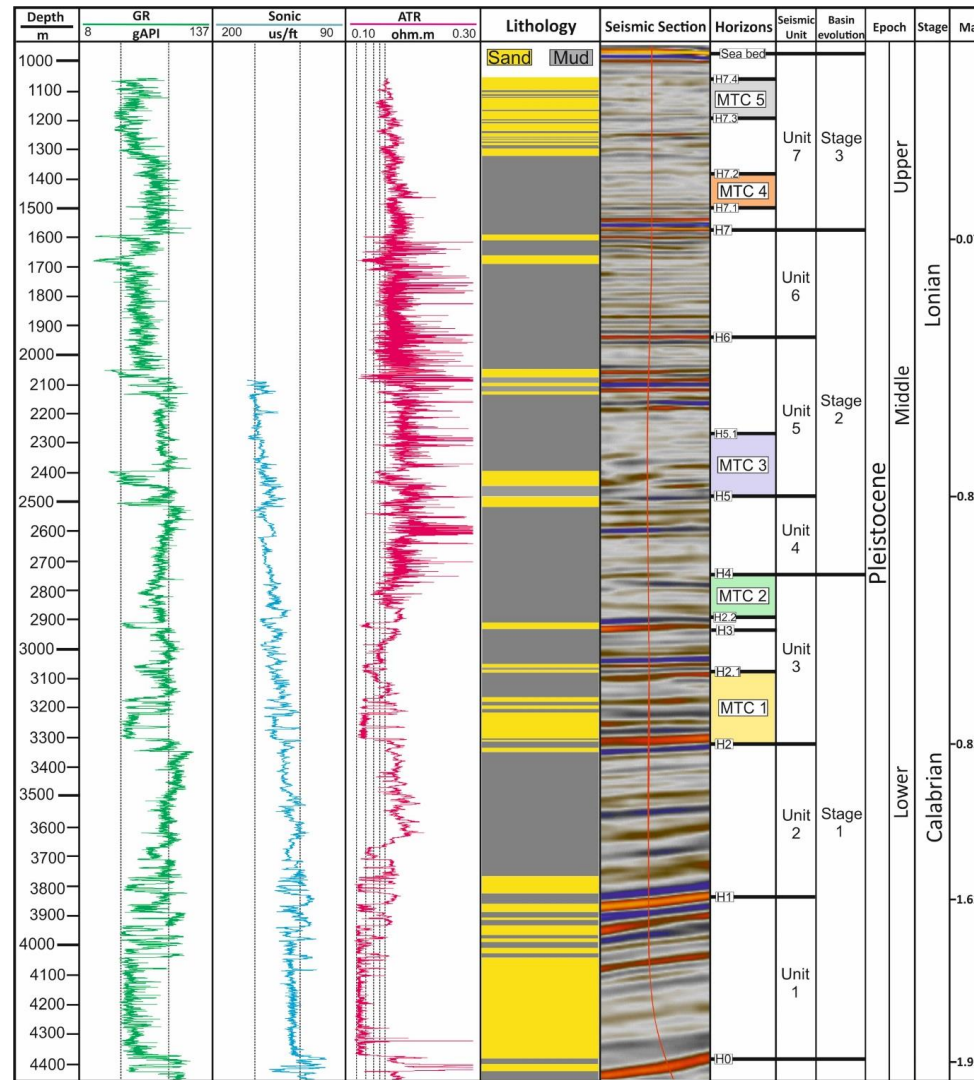


Figure 7a

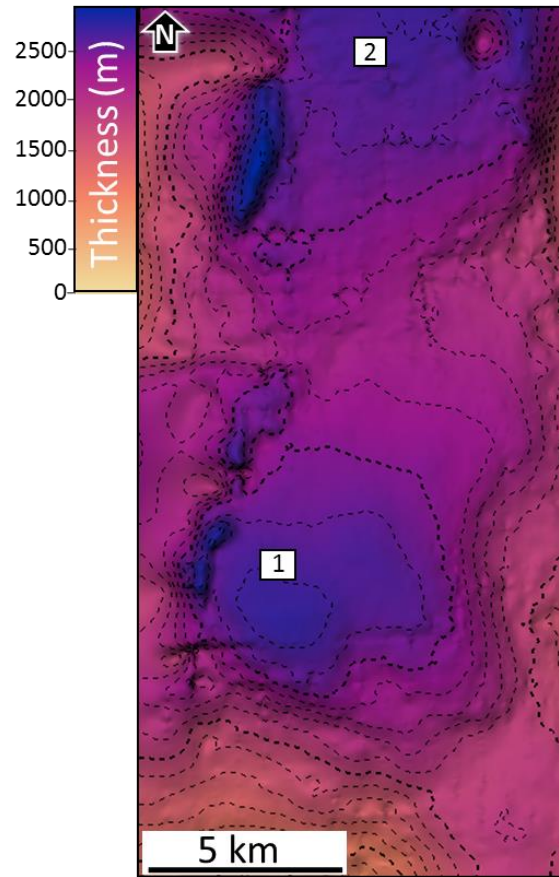


Figure 7b

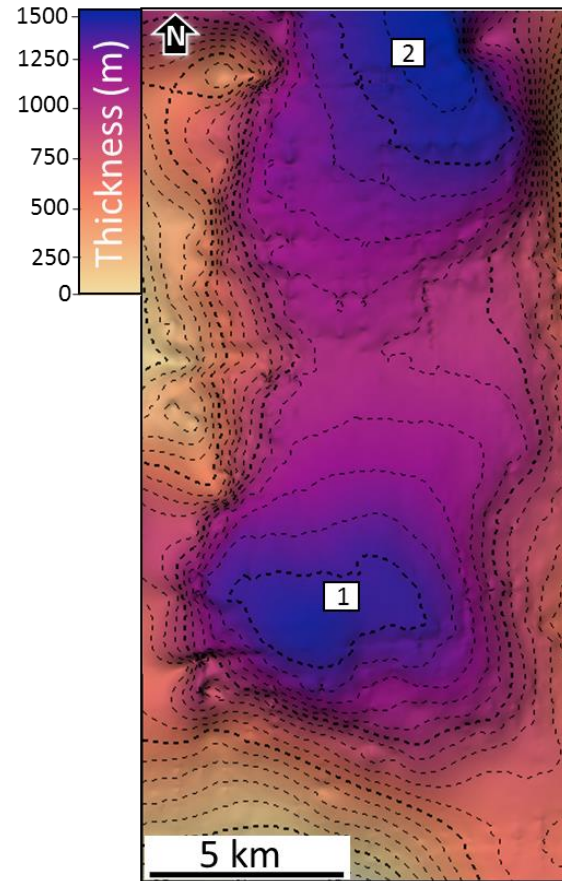


Figure 7c

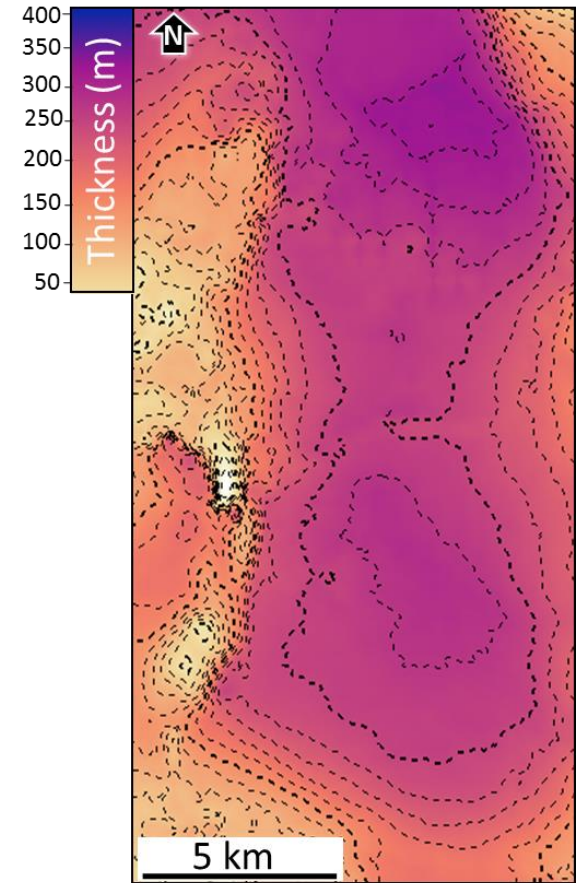


Figure 8a

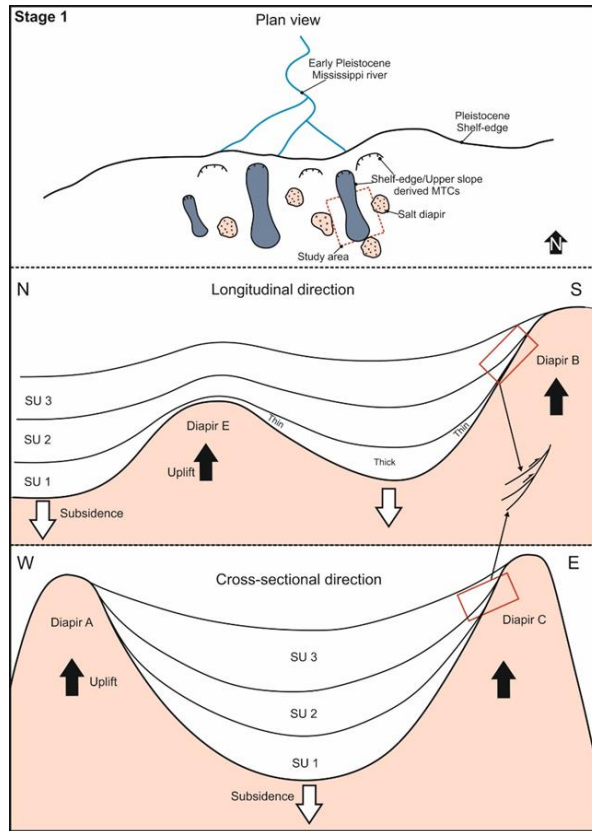


Figure 8b

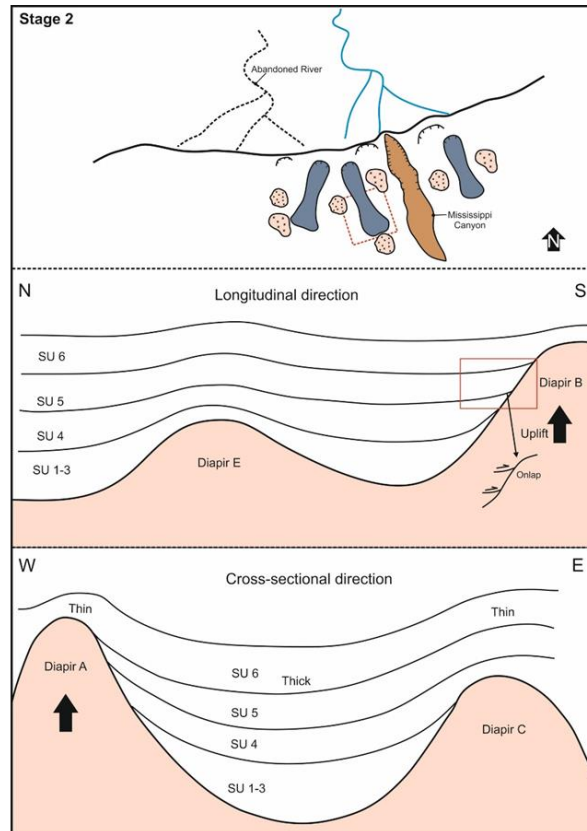


Figure 8c

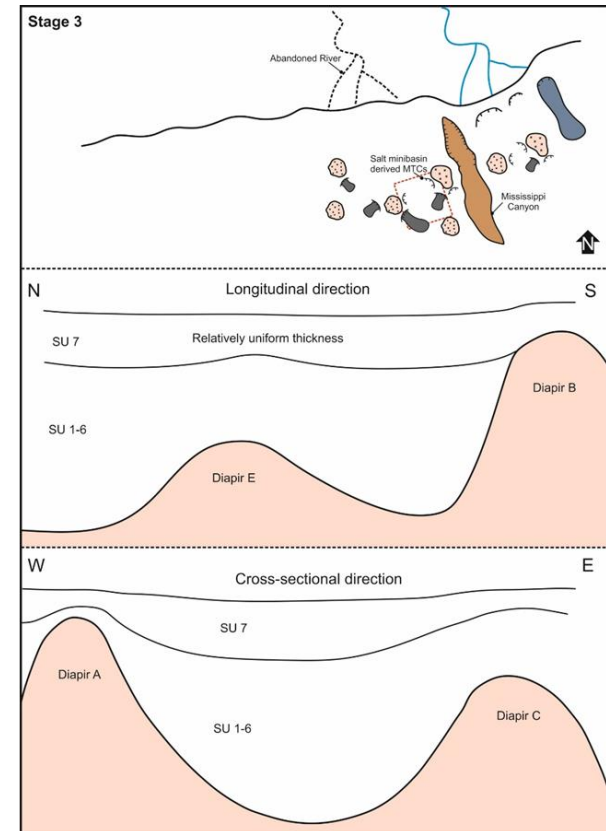


Figure 9

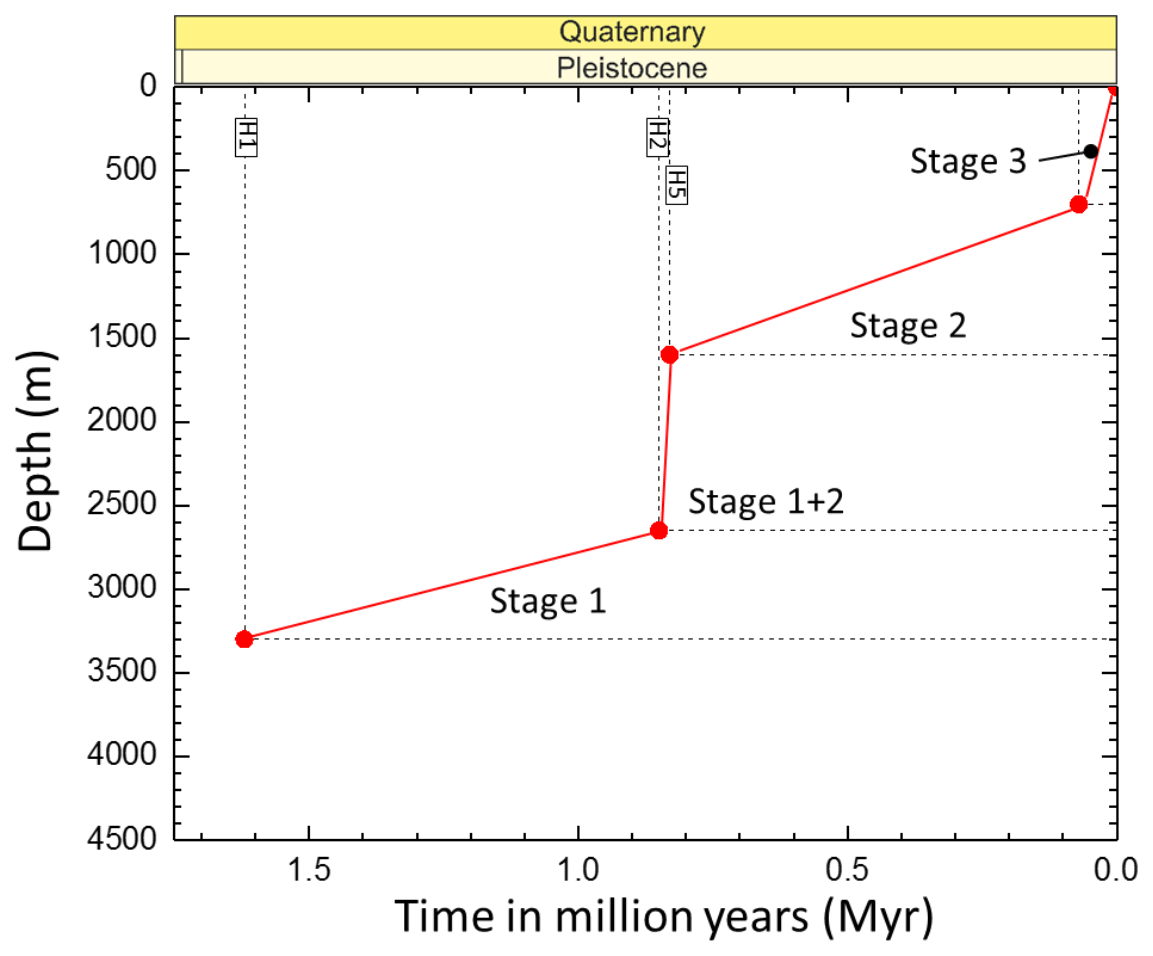


Figure 10a

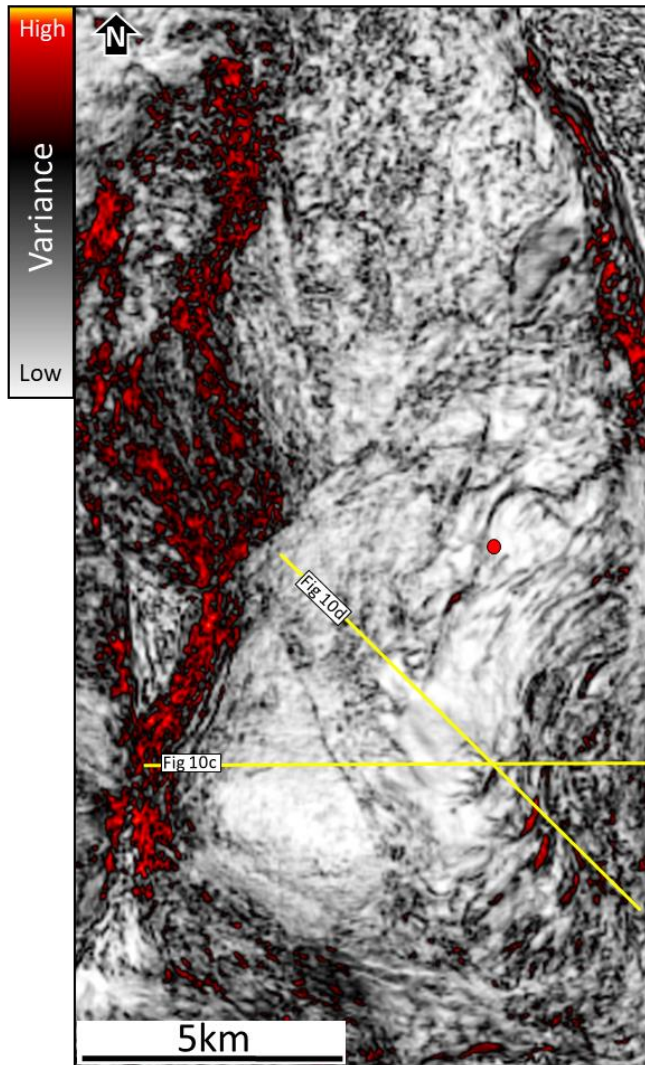


Figure 10b

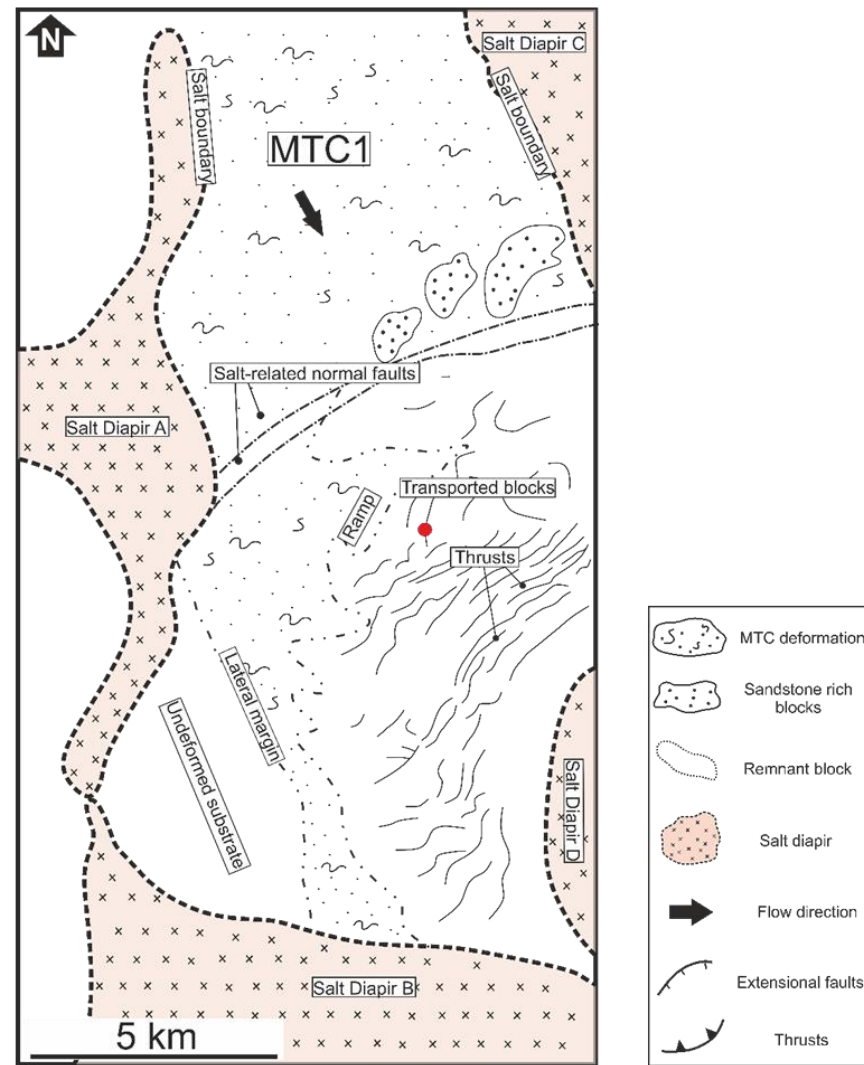


Figure 10c

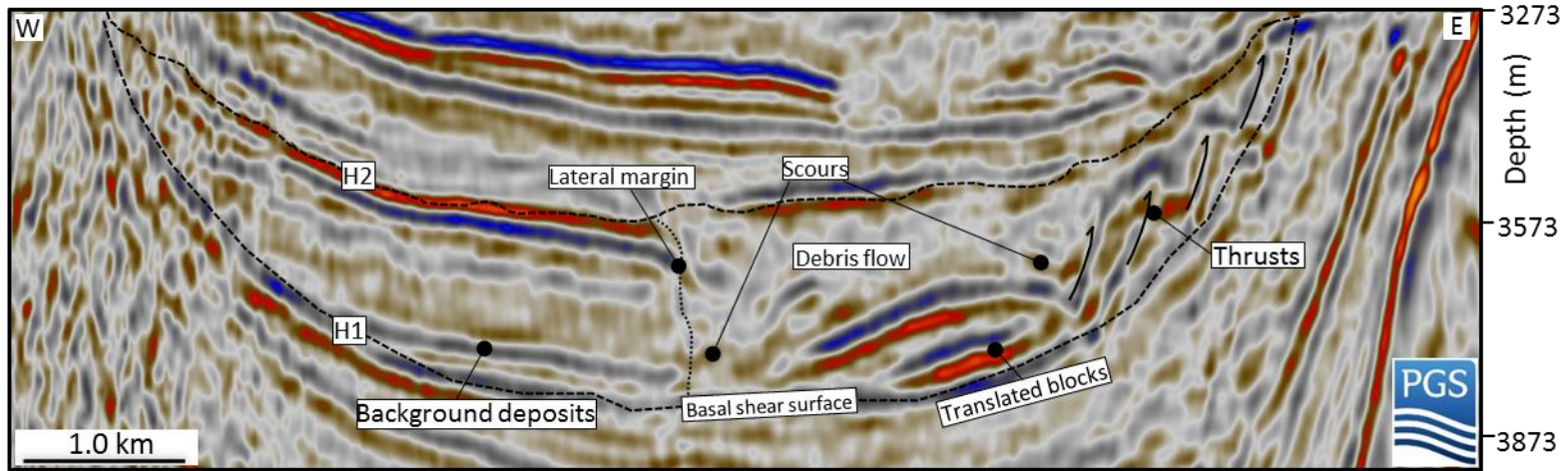


Figure 10d

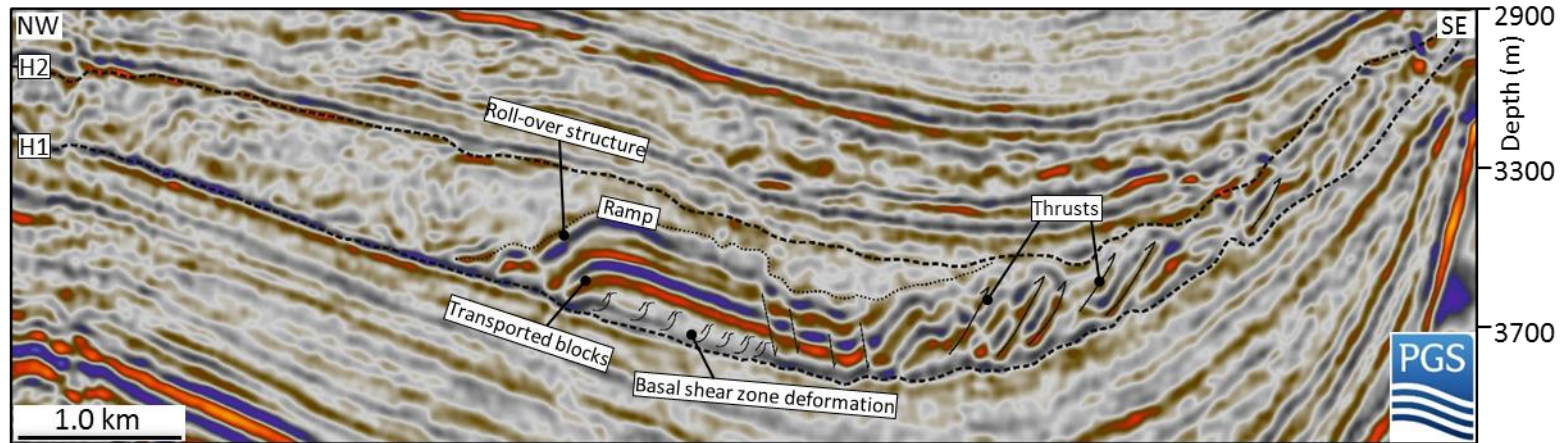


Figure 11a

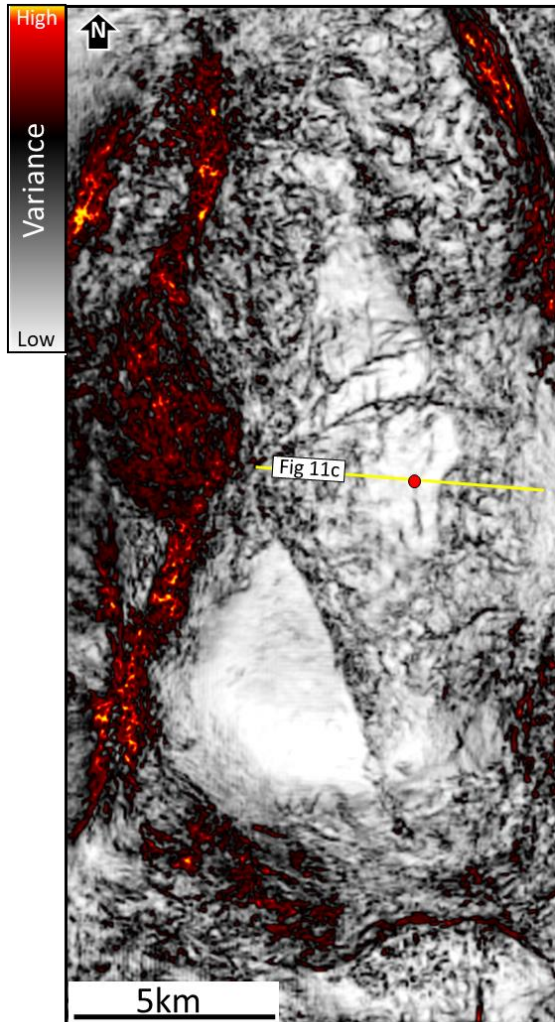


Figure 11b

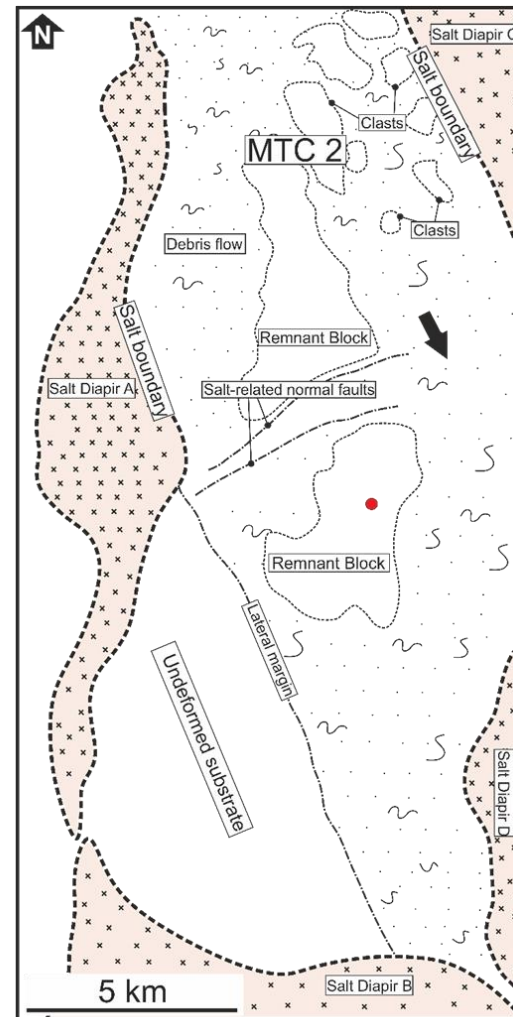


Figure 11c

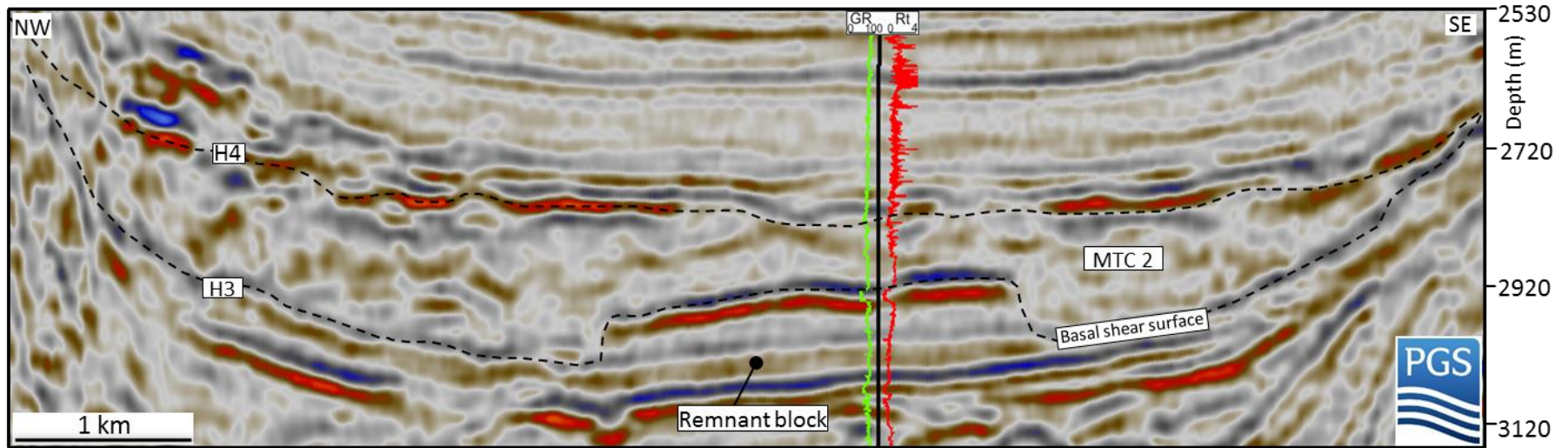


Figure 12a

Figure 12b

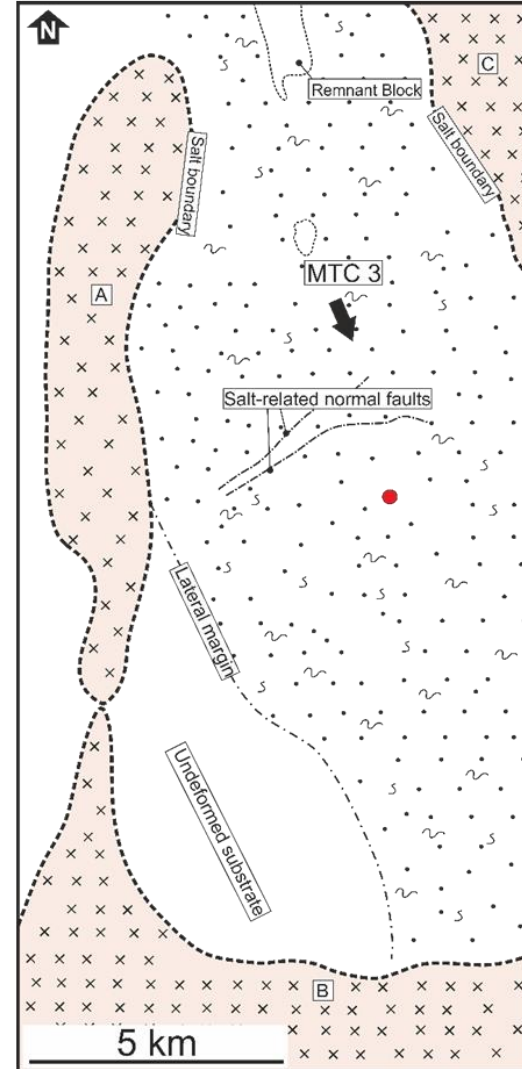
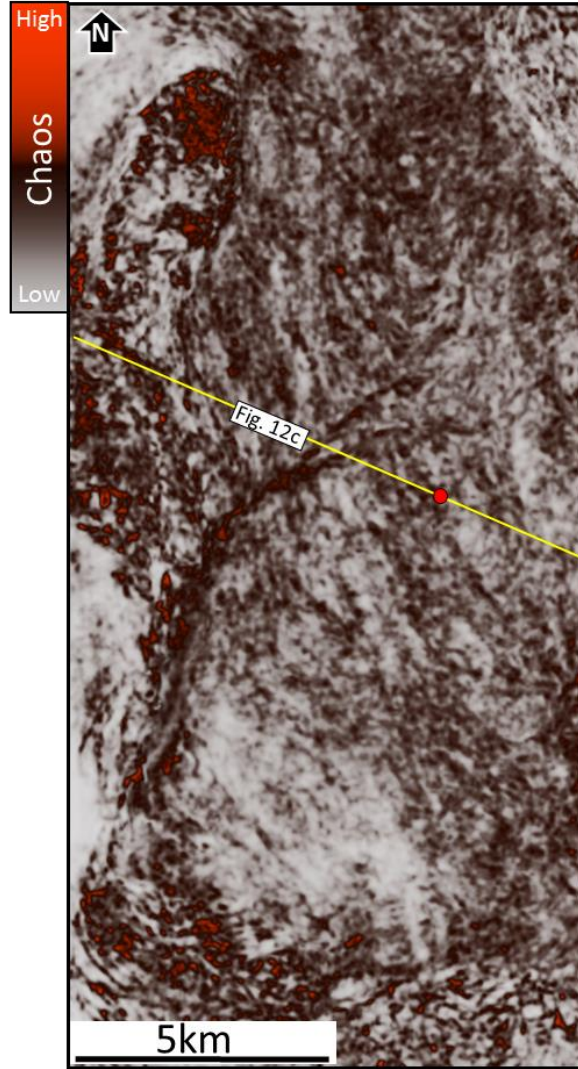


Figure 12c

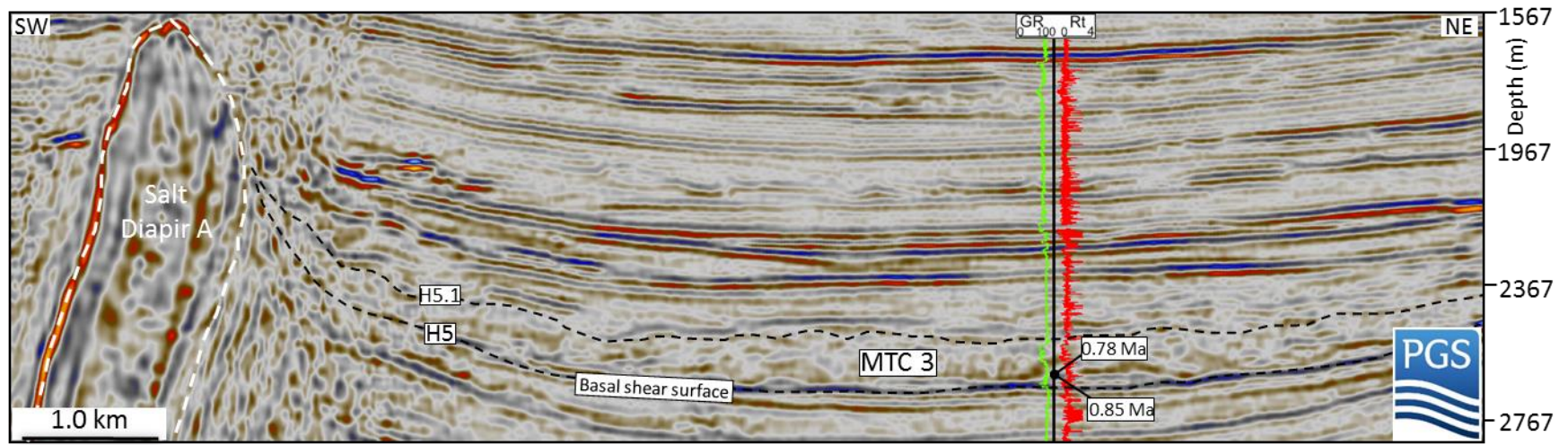


Figure 12d

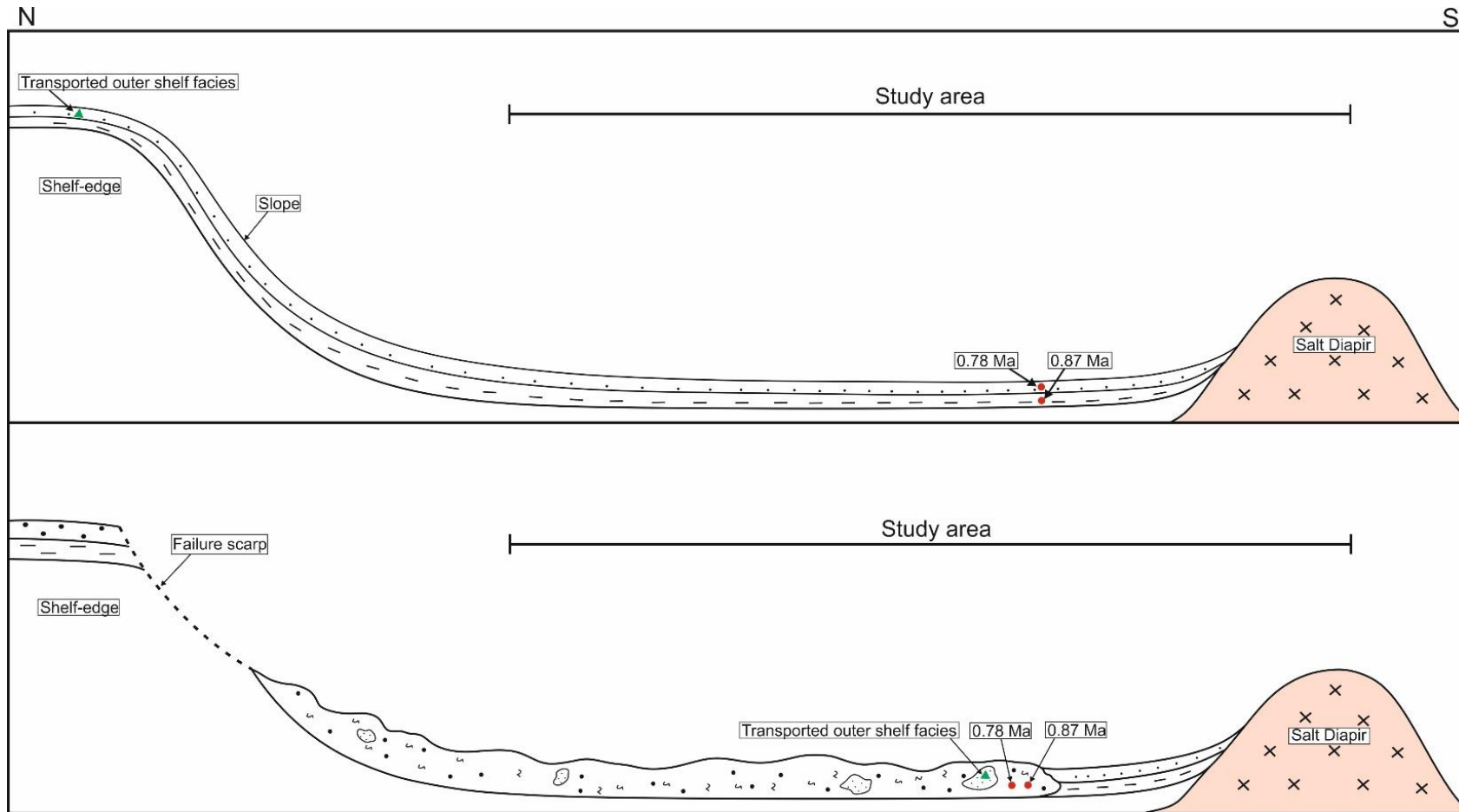


Figure 12e

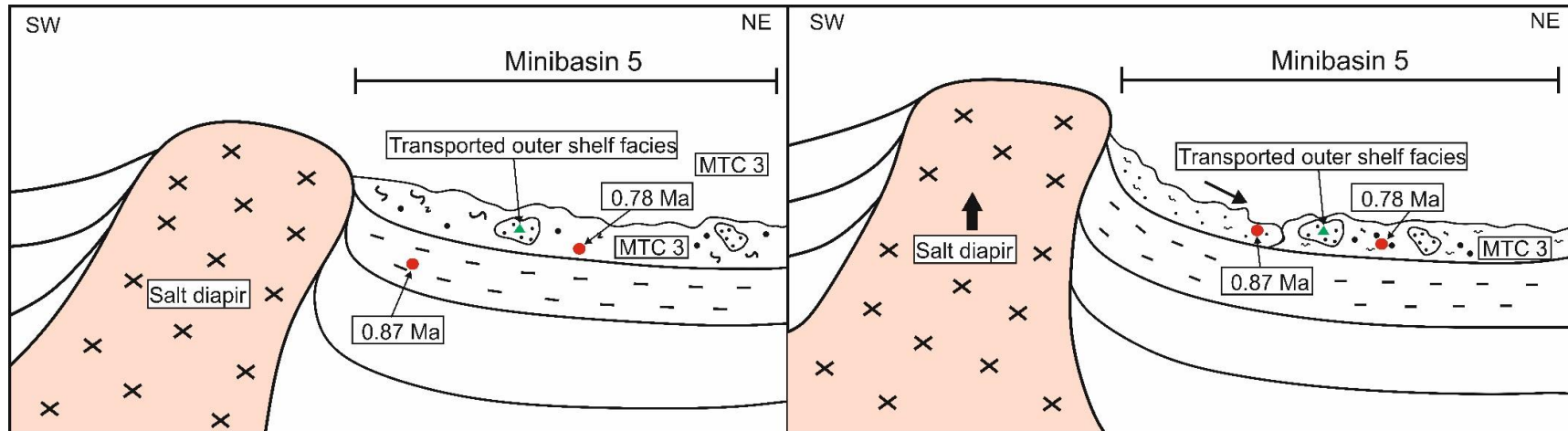


Figure 13

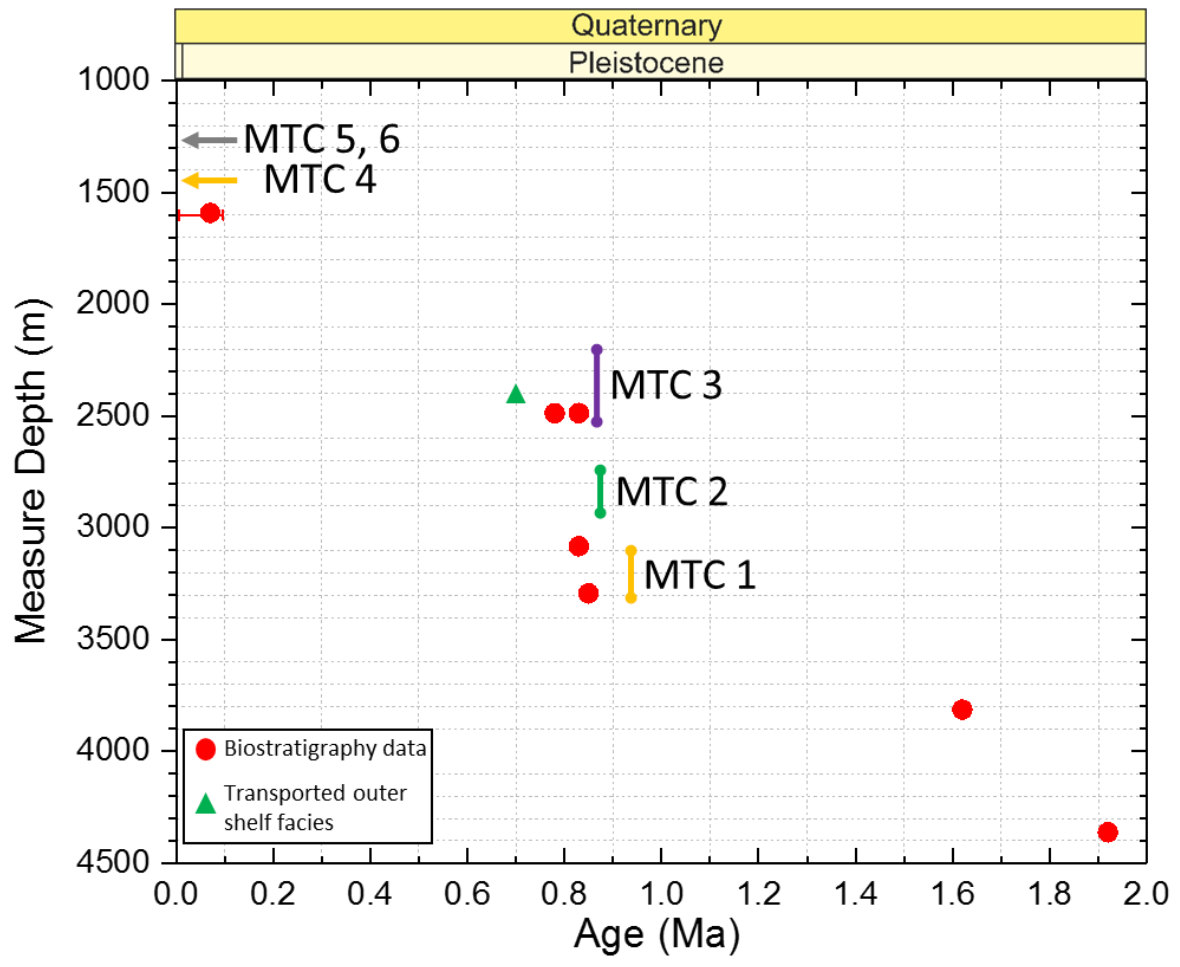


Figure 14a

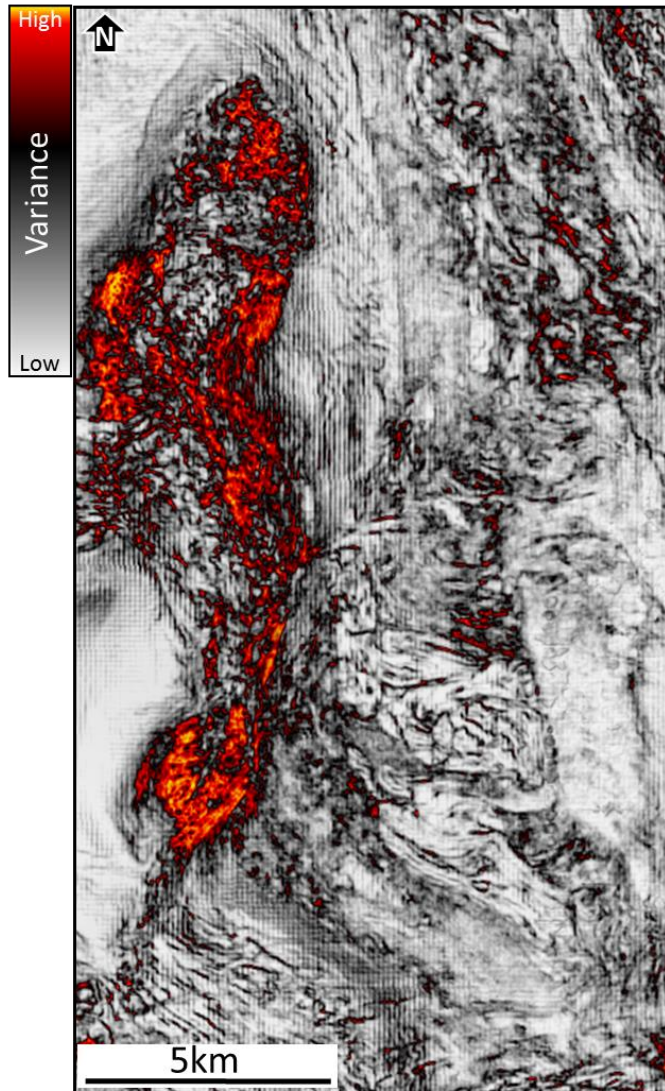


Figure 14b

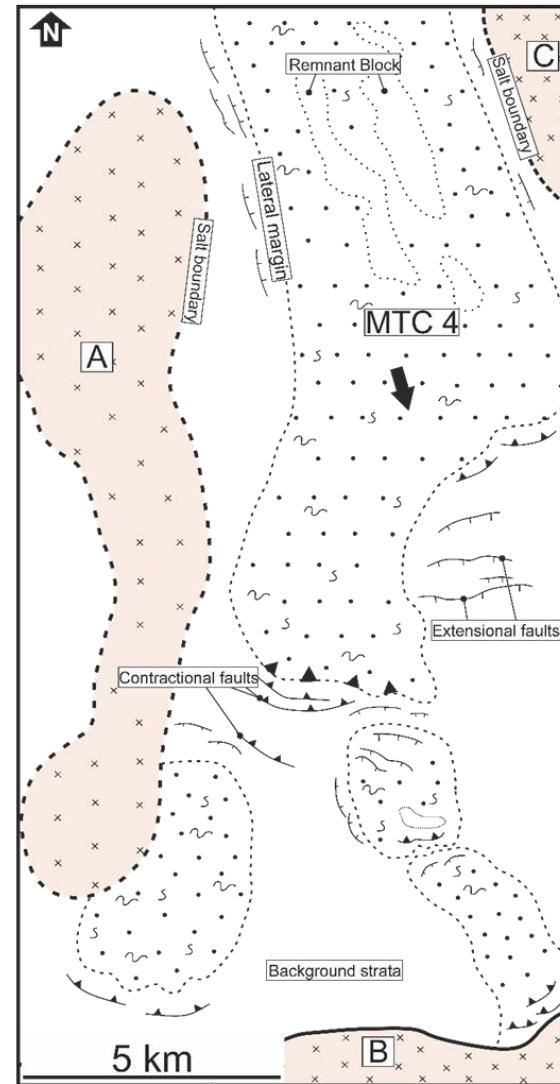


Figure 15a

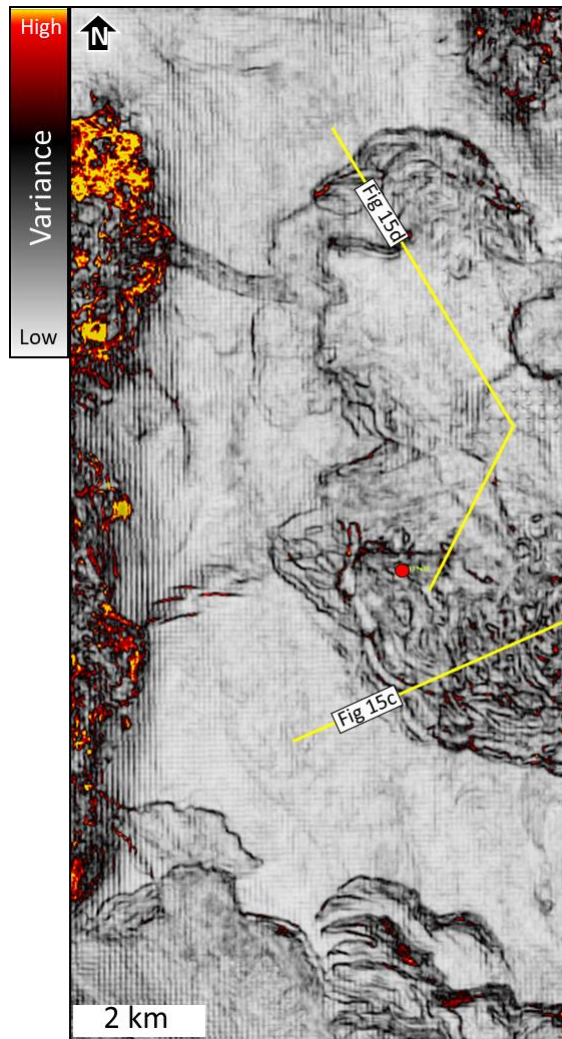


Figure 15b

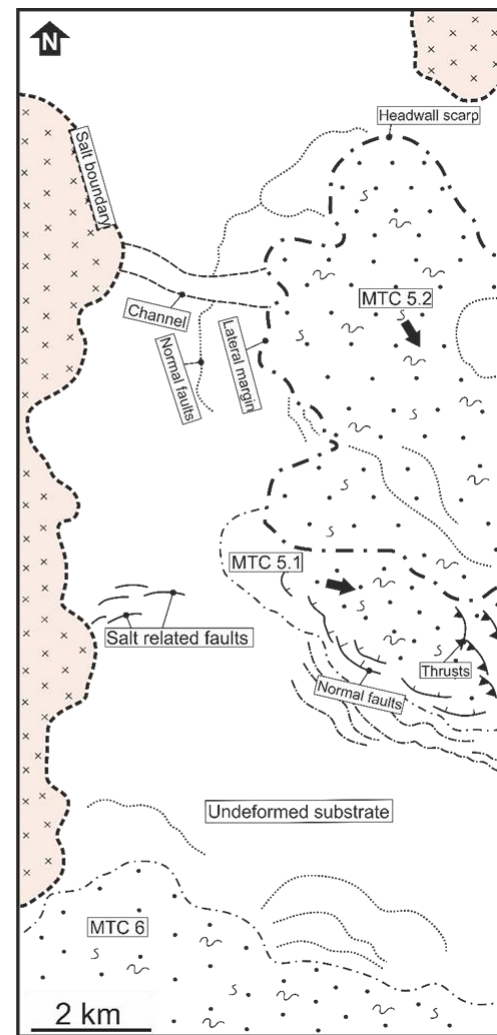


Figure15c

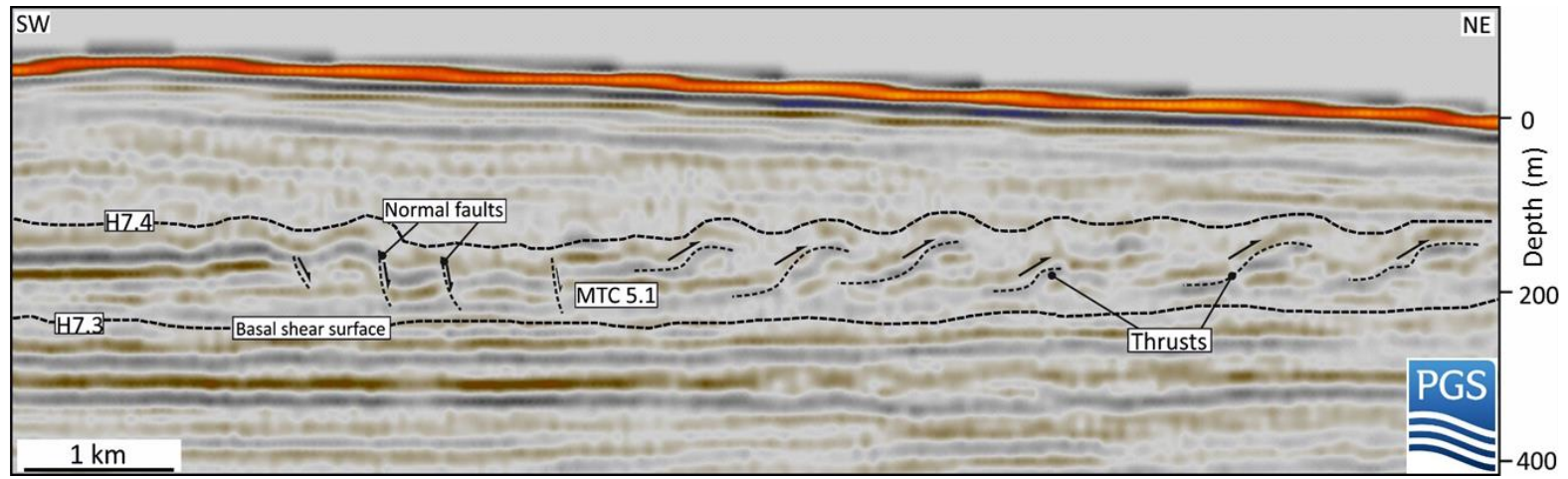


Figure 15d

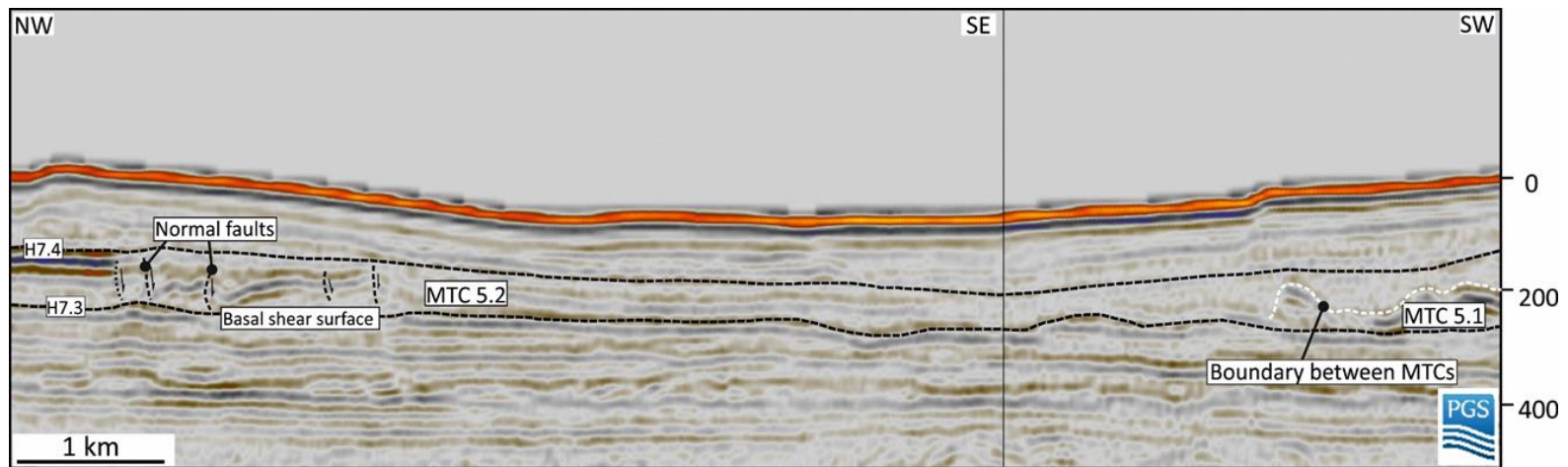


Figure 16a

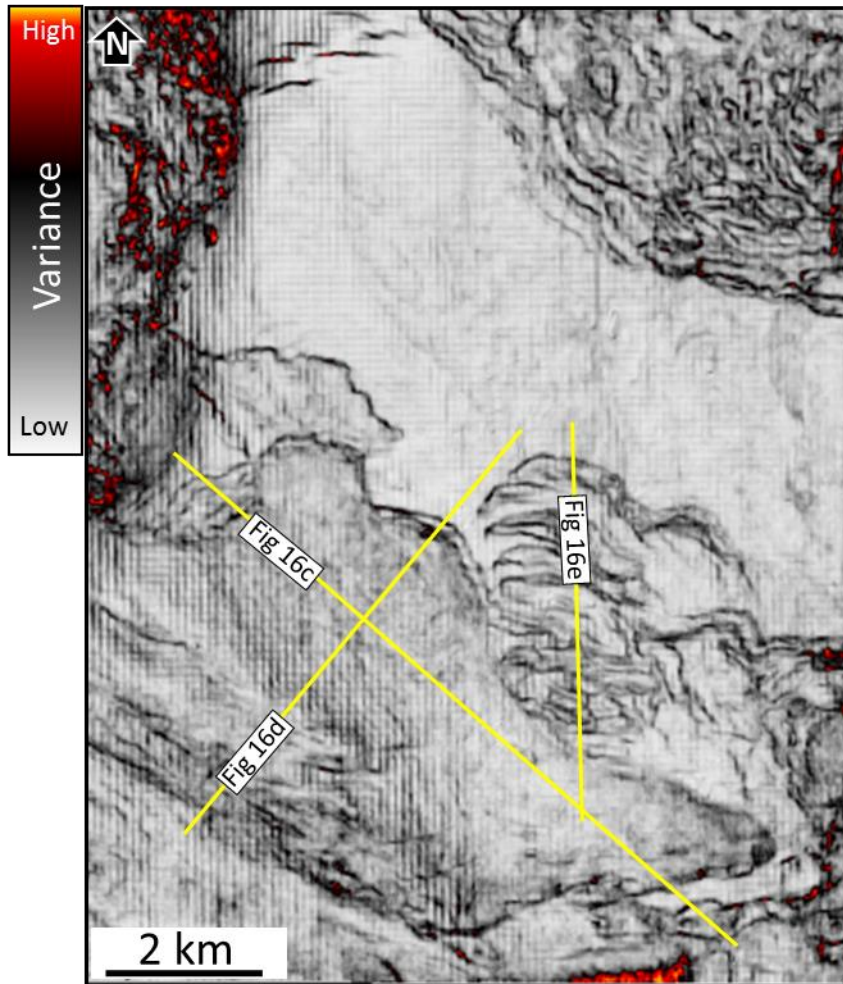


Figure 16b

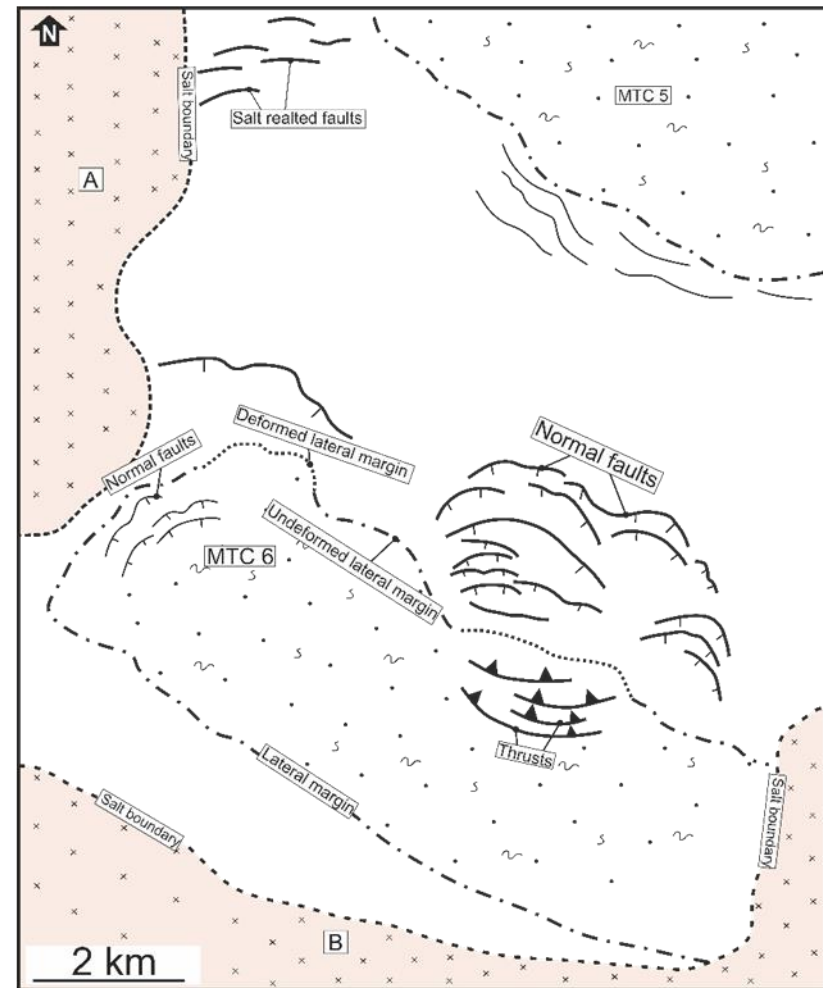


Figure 16c

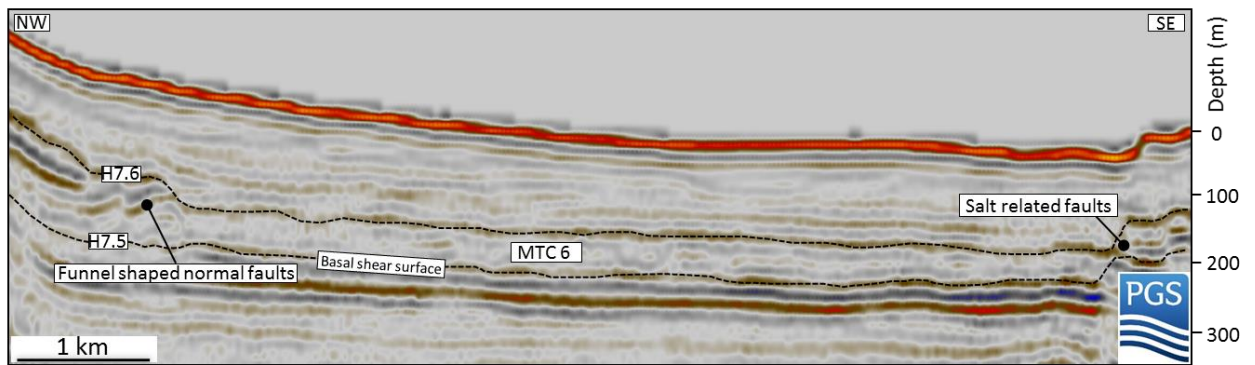


Figure 16d

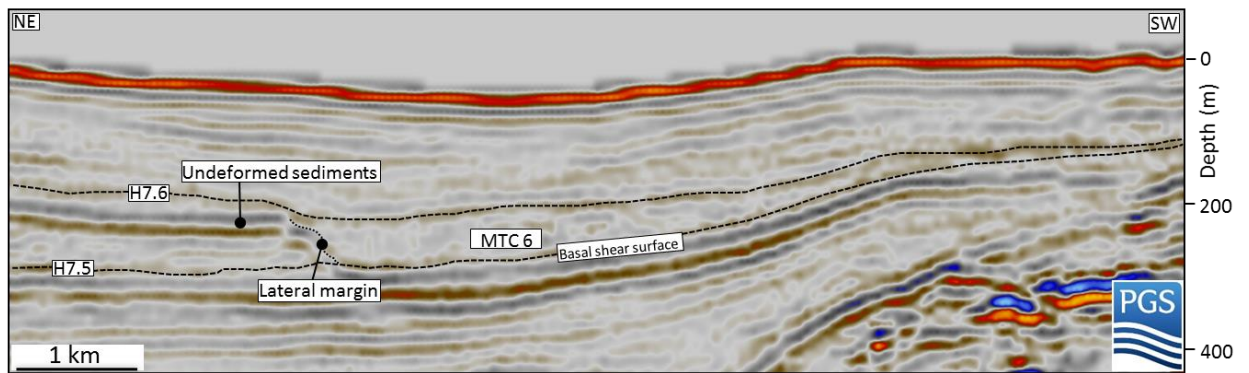


Figure 16e

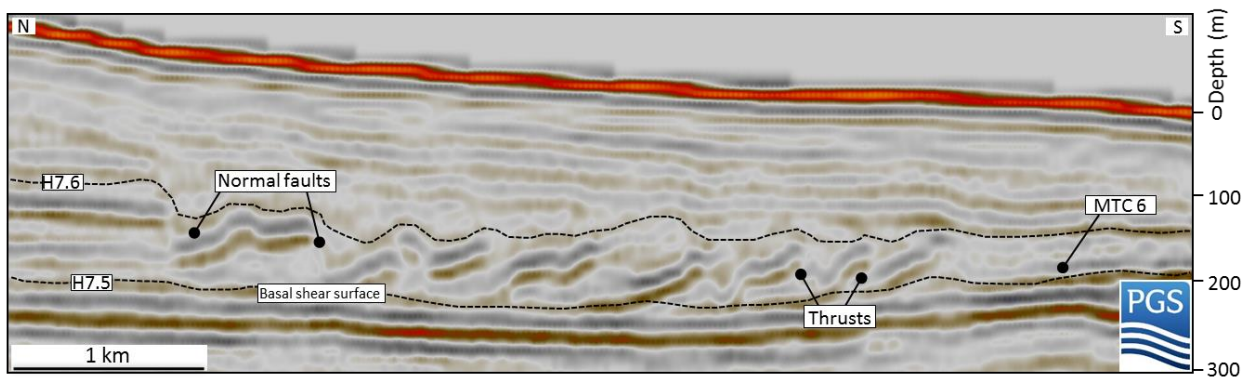


Figure 17a

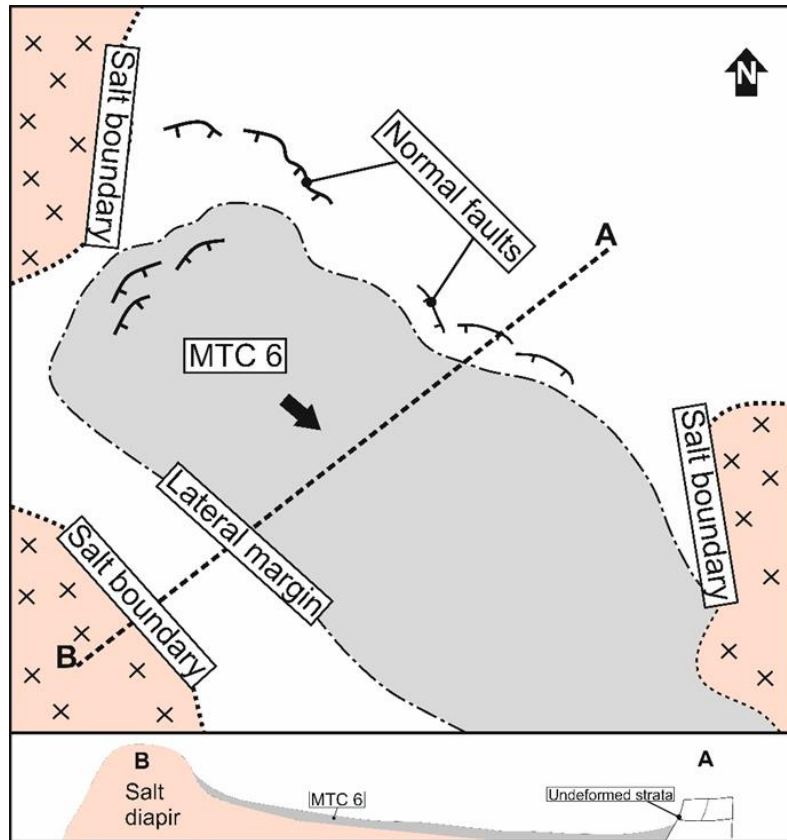


Figure 17b

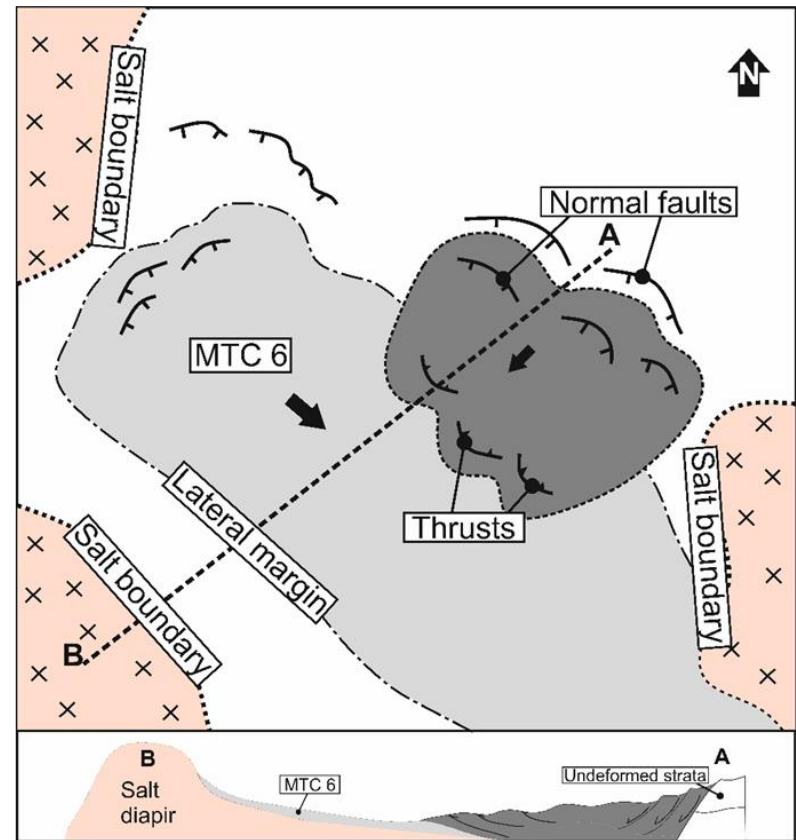


Figure 18

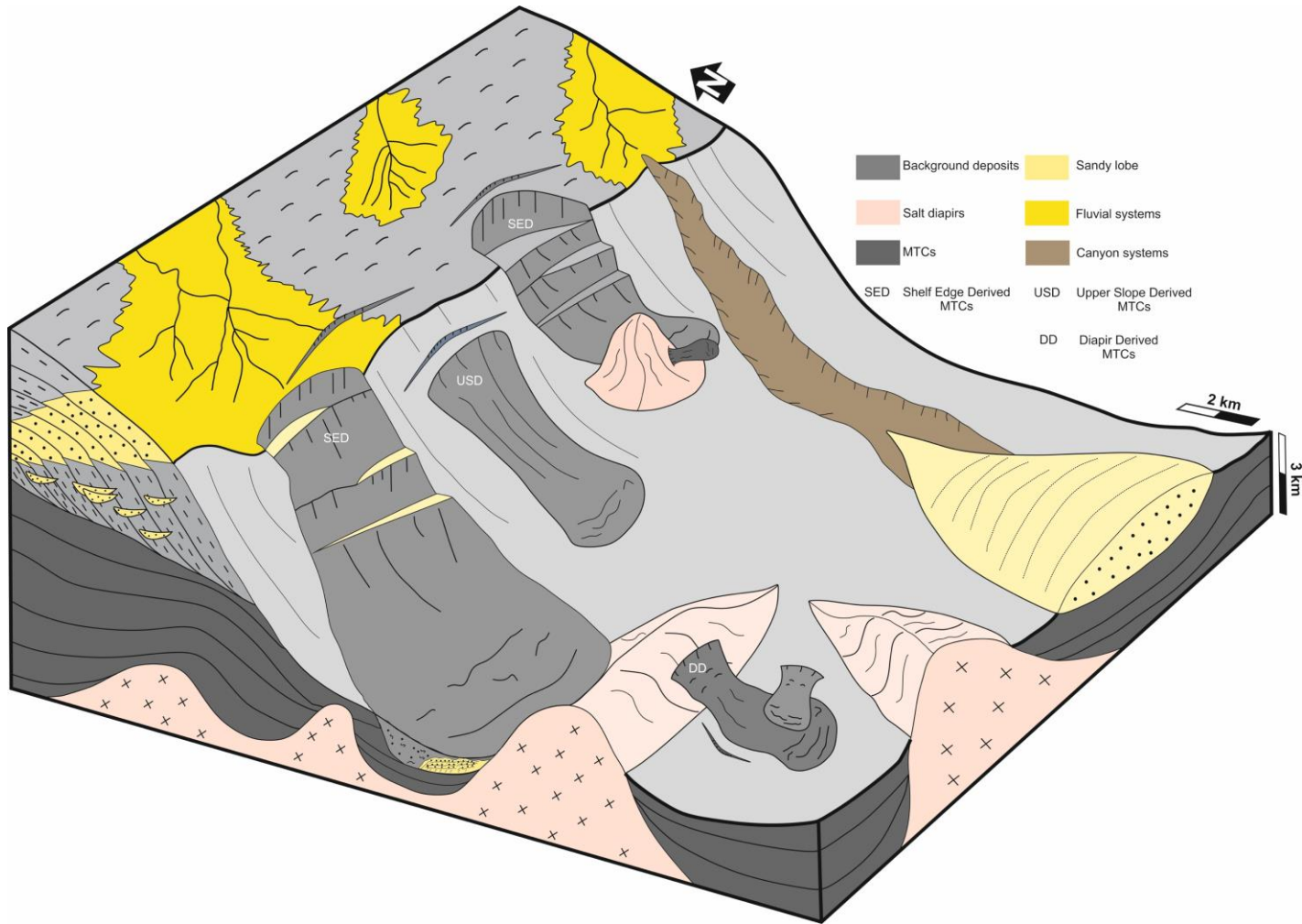


Figure 19

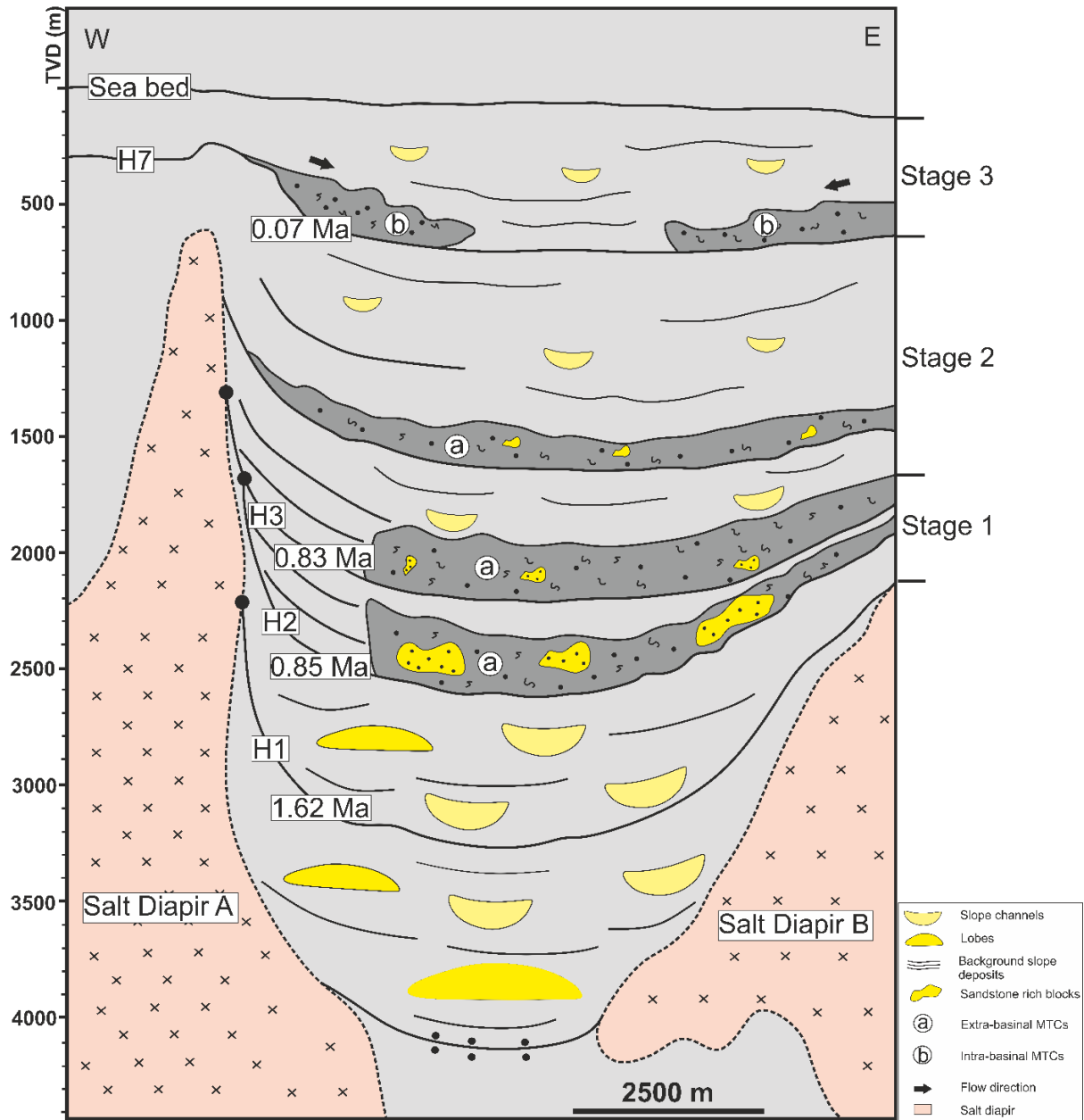


Figure 20

